Impact of Parameterized Internal Wave Drag on the Semidiurnal Energy Balance in a Global Ocean Circulation Model*

MAARTEN C. BUIJSMAN,[+] JOSEPH K. ANSONG,[#] BRIAN K. ARBIC,[#] JAMES G. RICHMAN,[@] JAY F. SHRIVER,[&] PATRICK G. TIMKO,[**] ALAN J. WALLCRAFT,[&] CAITLIN B. WHALEN,[++] AND ZHONGXIANG ZHAO[##]

[+] University of Southern Mississippi, Stennis Space Center, Mississippi
[#] University of Michigan, Ann Arbor, Michigan
[@] Center for Ocean-Atmospheric Prediction Studies, Florida State University, Tallahassee, Florida
[&] U.S. Naval Research Laboratory, Stennis Space Center, Mississippi
[**] Bangor University, Menai Bridge, Anglesey, United Kingdom
[++] Scripps Institution of Oceanography, University of California, San Diego, La Jolla, California
[##] Applied Physics Laboratory, University of Washington, Seattle, Washington

ABSTRACT

The effects of a parameterized linear internal wave drag on the semidiurnal barotropic and baroclinic energetics of a realistically forced, three-dimensional global ocean model are analyzed. Although the main purpose of the parameterization is to improve the surface tides, it also influences the internal tides. The relatively coarse resolution of the model of ~8 km only permits the generation and propagation of the first three vertical modes. Hence, this wave drag parameterization represents the energy conversion to and the subsequent breaking of the unresolved high modes. The total tidal energy input and the spatial distribution of the barotropic energy loss agree with the Ocean Topography Experiment (TOPEX)/Poseidon (TPXO) tidal inversion model. The wave drag overestimates the high-mode conversion at ocean ridges as measured against regional high-resolution models. The wave drag also damps the low-mode internal tides as they propagate away from their generation sites. Hence, it can be considered a scattering parameterization, causing more than 50% of the deep-water dissipation of the internal tides. In the near field, most of the baroclinic dissipation is attributed to viscous and numerical dissipation. The far-field decay of the simulated internal tides is in agreement with satellite altimetry and falls within the broad range of Argo-inferred dissipation rates. In the simulation, about 12% of the semidiurnal internal tide energy generated in deep water reaches the continental margins.

1. Introduction

Surface tides are generated at a rate of 3.5 TW (±5%; Egbert and Ray 2001; Buijsman et al. 2015), and as they propagate over rough underwater topography about 1 TW (±30%; Waterhouse et al. 2014; and references therein) of their energy is converted to baroclinic tidal waves (internal tides), which eventually break and dissipate. The diapycnal mixing associated with the breaking internal tides may provide up to half the energy that maintains the meridional overturning circulation (Munk and Wunsch 1998). Global barotropic tide models cannot simulate this energy transfer implicitly. Hence, a parameterized internal wave drag that accounts for this energy transfer needs to be applied to correctly predict tidal water levels in forward barotropic tide models (e.g., Jayne and St. Laurent 2001; Egbert et al. 2004; Lyard et al. 2006; Green and Nycander 2013; Buijsman et al. 2015). Wave drag schemes, such as by Jayne and St. Laurent (2001), Garner (2005), Nycander (2005), and Falahat et al. (2014), are based on the linear theory discussed by Bell (1975) and Stigebrandt (1999). The wave drag depends on the topographic roughness, stratification, and tidal and Coriolis frequencies.

While forward, global, barotropic tide models require a wave drag parameterization for optimal performance, simulations with global, forward, three-dimensional (3D) tide models have been performed both with wave drag

(Arbic et al. 2004, 2010, 2012) and without it (Simmons et al. 2004a; Müller et al. 2012). Niwa and Hibiya (2011, 2014) also run global 3D tide models without wave drag, but they assimilate tidal elevations and apply a linear drag on the tidal baroclinic velocities. The application of a parameterized, tidal, internal wave drag in a global baroclinic tide model is somewhat counterintuitive because internal waves are generated in such models. However, poorly resolved bathymetry and the relatively coarse horizontal resolution in most of these models (typically of order 10 km) tends to limit the generation and propagation to the lowest vertical modes, which have wave lengths of at least 50 km. Hence, high vertical mode waves, which appear in the real ocean, are unresolved in these models.

Arbic et al. (2004) performed global one- and two-layer tide-only simulations with the Hallberg isopycnal model (HIM; Hallberg and Rhines 1996). Arbic et al. (2004) found that the wave drag required to achieve accurate surface water levels in two-layer tide simulations had nearly the same strength as the drag needed in one-layer simulations. For their tuned two-layer simulations, Arbic et al. (2004) found a root-mean-square (RMS) water-level error with an altimetry-constrained model of 7.3 cm for the semidiurnal lunar tide M_2. Arbic et al. (2004, p. 3082) reasoned that "it is computationally infeasible for our hydrostatic, two-layer model to resolve the generation and breaking of internal waves at very small scales. Hence the need apparently remains for parameterized drag, which we have acting on the lower-layer flow rather than the barotropic flow." Simmons et al. (2004a) did not apply a wave drag scheme in their global, two-layer HIM model, similarly set up as in Arbic et al. (2004), and found an RMS error of 23.4 cm (Arbic et al. 2010), illustrating the need for these drag schemes in baroclinic tide models. Arbic et al. (2010) performed simulations of the 3D global Hybrid Coordinate Ocean Model (HYCOM; Bleck 2002) with tidal and atmospheric forcing. As in Arbic et al. (2004), they applied the linear internal wave drag scheme of Garner (2005) to the bottom velocities, which are dominated by the barotropic and low baroclinic modes, and used the same drag strength as in separately tuned barotropic tide experiments. The wave drag tuning was not repeated with the baroclinic model because of its much greater computational expense. The 3D simulation yielded similar water-level RMS errors as in the barotropic experiment. In this paper, we analyze a HYCOM simulation, hereafter referred to as the 18.5 solution, which represents an improvement over the original HYCOM baroclinic tides simulation reported on by Arbic et al. (2010); see Shriver et al. (2012) for details and Arbic et al. (2012) for an overview of the 18.5 solution.

Three-dimensional global models with realistic tidal and atmospheric forcing are valuable tools to help us better understand the internal tide generation, propagation, interaction with the mesoscale flow field, and dissipation. After generation, low-mode internal tides may propagate for 1000s of km (Ray and Mitchum 1997). An area of active research aims to determine where and how much internal tidal energy is lost along the way. Internal tides may cascade to turbulence at the generation sites through lee-wave breaking (Legg and Klymak 2008; Klymak et al. 2008; Buijsman et al. 2012); scatter to higher modes that eventually dissipate through wave–wave interaction (Polzin 2004; MacKinnon et al. 2013; Eden and Olbers 2014), through topographic interaction (Mathur et al. 2014; and references therein), or through interaction with eddies (Dunphy and Lamb 2014; Kerry et al. 2014); or internal tides may dissipate by shoaling and breaking at remote coastal shelf topography (Nash et al. 2004; Martini et al. 2011; Kelly et al. 2013; Alford et al. 2015). Waterhouse et al. (2014) computed dissipation rates from numerous oceanographic measurements and found bottom-enhanced dissipation rates over rough topography, indicative of internal tide dissipation. They compared these rates with the low-mode internal tide power input from a ⅛° global ocean model and estimated that about 31% of the deep-water internal tides reaches the continental margins.

The discussion above shows that baroclinic tide models need an internal wave drag parameterization to account for the tidal energy conversion from the barotropic to the unresolved high vertical modes. Moreover, they also require a parameterization to represent the energy loss to breaking internal tides. For example, Niwa and Hibiya (2014) found that without the application of linear damping terms, the magnitude of the far-field internal tides was too large. In HYCOM the linear wave drag parameterization suits a dual purpose, that is, it drags on both the barotropic and baroclinic tides. However, the effect of this drag on the near- and far-field internal tide dissipation is not well understood. Recently, Ansong et al. (2015) performed a series of global HYCOM simulations for the M_2 tide in an eddying ocean and found that the surface and internal tides agreed best with the Ocean Topography Experiment (TOPEX)/Poseidon (TPXO) tidal inversion model (Egbert et al. 1994) and altimetry when a linear wave drag with a certain amplification factor was applied. These findings are in agreement with the (internal) tidal energy balance analysis presented here.

In this paper, one objective is to study the impact of parameterized internal wave drag on the internal tide energetics. How does the wave drag affect the internal tide decay? How much energy reaches the shelves? A

second objective is to study the effect of the wave drag on the barotropic tidal energetics. Does the wave drag correctly simulate the unresolved energy conversion to high wave modes? To date, the analysis of the surface and internal tides in the 18.5 solution has mainly focused on the sea surface height (Shriver et al. 2012, 2014), but the barotropic and baroclinic tidal energetics of HYCOM have not yet been documented.

We proceed in the next section with a discussion of the HYCOM 18.5 simulation and the methodology of the analysis. In the results section, we consider the global and regional tidal barotropic and baroclinic energy balances. We evaluate the relative importance of the wave drag for tall and steep ridges and for deep and flat midocean spreading ridges. At these two types of generation sites we study how well the linear wave drag represents the conversion to high-mode energy. We compare the depth-averaged far-field internal tide dissipation in HYCOM with dissipation inferred from Argo floats and altimetry. We estimate how much low-mode energy reaches the shelves in HYCOM. We end with a discussion and conclusions.

2. Methods

a. HYCOM

The HYCOM 18.5 simulation has geopotential tidal forcing for the four largest semidiurnal constituents (M_2, S_2, N_2, and K_2) and diurnal constituents (K_1, O_1, P_1, and Q_1), a scalar self-attraction and loading correction (SAL; Ray 1998), 32 layers in the vertical direction, and a nominal horizontal resolution of $1/12.5°$ at the equator. Apart from the tidal forcing, the model setup is the same as for the nontidal global model discussed in Metzger et al. (2010). The model is run interannually over the period of July 2003–December 2010 using 3-h Fleet Numerical Meteorology and Oceanography Center (FNMOC) Navy Operational Global Atmospheric Prediction System (NOGAPS) atmospheric forcing with wind speeds scaled to be consistent with QuikSCAT observations (Rosmond et al. 2002). No tidal data are assimilated into the simulation. This paper analyzes one-hourly, three-dimensional global fields that have been stored for a 30-day period starting at midnight on 2 September 2004.

As in Arbic et al. (2010), the 18.5 solution utilizes the tensor wave drag by Garner (2005) in a scalarized form. The main purpose of the wave drag is to improve the surface tides in HYCOM. In this paper, we show that the drag also affects the internal tides. The drag strength is a function of topographic roughness, bottom stratification, tidal and Coriolis frequencies, and a topographic Froude number to account for topographic blocking. See Arbic et al. (2010) for a detailed explanation of the

wave drag implementation in HYCOM. The internal wave drag is applied in the bottom 500 m and is independent of depth over this layer. This vertical length scale is adopted from St. Laurent et al. (2002), who, on the basis of turbulence measurements, approximated 500 m to be the vertical decay scale for turbulence due to breaking internal waves over rough topography. The drag is meant to be applied to the tidal flow. However, we cannot instantaneously separate the tidal from the nontidal flows. In a first step, the drag is applied to the total flow field. In a second corrective step, an "anti-drag" is applied to the subtidal flow, which is extracted from the total flow fields using a 25-h lagged boxcar filter and averaged over the bottom 500 m. This filter removes 97.4% of the tides. In this second step, we assume that the subtidal flow is independent of depth. In shallow water <500-m subtidal currents are strong and have significant vertical structure, invalidating this assumption. To avoid the spinup of spurious residual currents that may result from the tidal/subtidal separation method (Arbic et al. 2010), the drag strength is set to zero for grid points having seafloor depths shallower than 500 m and is linearly increased to full strength for seafloor depths greater than 1000 m. The minimum e-folding time scale equals 24 h, after an amplification factor of 12 is applied.

This choice of depth below which the wave drag is applied may affect the tidal energetics, although we do not have twin experiments of the 18.5 solution to test this. The coupling between the wave drag and the surface and internal tides is very nonlinear. If the linear wave drag were to be applied at full strength everywhere, the tidal water levels and internal tides would also change. Hence, the wave drag needs to be tuned again in order to get the most optimal tidal water levels (Buijsman et al. 2015), which may be different than for the 18.5 solution. Buijsman et al. (2015) performed a series of global barotropic tide simulations for different wave drag parameterizations. They found that the application of the full wave drag increased the wave drag dissipation in shallow water relative to deep water. To correctly quantify the effects of an altered wave drag, new 3D simulations are required, which are computationally expensive.

The 18.5 solution has been thoroughly compared with observations. Shriver et al. (2012) compared the surface elevation expression of the barotropic and baroclinic tides with altimetry and found that the simulated and observed coherent internal tide amplitudes, spatially averaged over the generation regions, agreed to approximately 15% for the four largest semidiurnal constituents and 23% for the four largest diurnal constituents. In Timko et al. (2012, 2013), HYCOM tidal

currents are compared with historic current meter records. It was found that HYCOM has reasonable skill in reproducing the vertical structure of tidal kinetic energy.

b. Analysis

In this analysis, we focus on the semidiurnal tidal band, as it contains about 85% of the total energy input to the tides (Egbert and Ray 2003). We apply a bandpass filter with a cutoff period between 9 and 15 h to the sea surface height, barotropic and baroclinic velocities, and the layer thicknesses. The bandpassed variables are used to compute the energetics, discussed in the next section. The density is assumed constant within each layer. This is certainly a valid assumption in the abyssal ocean where layer densities are little affected by mixing. In the mixed layer and near regions with strong convection, HYCOM switches to z coordinates, and the density within layers may change as a function of time. However, these areas are generally well mixed with small vertical density gradients and weak internal waves. The advantage of bandpassing is that both the coherent and incoherent tidal signals are obtained. This allows us to study the far-field dissipation of the internal tides.

To compare our model results with altimetry, we extract M_2 tides from these bandpassed fields using a least squares harmonic analysis in some cases. In this method, only the coherent tide is retained. Hence, one should be careful associating the amplitude decay of the M_2 internal tides strictly with dissipation. The decay may also be attributed to the incoherence of the internal tide (Zaron and Egbert 2014; Shriver et al. 2014; Ponte and Klein 2015).

c. Energetics

We analyze globally and regionally integrated and time-mean barotropic and baroclinic energy balances for the semidiurnal tidal bands. The global depth-integrated and time-mean barotropic (subscript 0) energy balance is

$$\{P\} = \{C + D_{w0} + D_{b0} + \mathcal{R}_0\} \tag{1}$$

(Egbert and Ray 2001; Simmons et al. 2004a; Kang and Fringer 2012), where { } indicates the area integral or area averaging, P is the tidal energy input, C is the conversion of barotropic energy to resolved baroclinic low vertical modes, D_{w0} is the unresolved barotropic to high-mode conversion, D_{b0} is the dissipation of barotropic energy due to quadratic bottom drag, $\mathcal{R}_0$ is a residual term accounting for discretization errors and numerical and viscous dissipation, and subscripts w and b refer to wave drag and bottom drag, respectively. Note that we have omitted the energy flux divergence, which integrates to zero in a global balance.

The global and regional area and depth-integrated and time-mean baroclinic energy balance for the resolved low vertical modes (subscript l) reads

$$\{C\} = \{\nabla \cdot \mathbf{F} + D_l\} \tag{2}$$

(Simmons et al. 2004a; Kang and Fringer 2012), where

$$\{D_l\} = \{D_{wl} + D_{bl} + \mathcal{R}_l\}, \quad \text{and} \tag{3}$$

$\mathbf{F} = (F_x, F_y)$ is the depth-integrated baroclinic pressure flux vector along the x and y coordinates, D_l is the low-mode dissipation, D_{wl} is baroclinic dissipation due to linear wave drag, D_{bl} is the dissipation due to bottom drag, and $\mathcal{R}_l$ is a residual term accounting for discretization errors and unresolved dissipation due to viscosity and the nonlinear coupling between the semidiurnal tides and other oceanic motions. The viscous damping cannot be computed directly because the eddy viscosity values were not stored. The nonlinear terms, such as the energy advection, in the baroclinic energy balance are ignored because they are at least an order of magnitude smaller for this ~8-km resolution and when globally integrated (Simmons et al. 2004a).

The time-mean and globally integrated tidal energy input in Eq. (1) is

$$\{P\} = \left\{ \left\langle g\rho_0 \eta_{\mathrm{EQ}} \frac{\partial \eta}{\partial t} \right\rangle \right\} \tag{4}$$

(Egbert and Ray 2001), where g is the gravitational acceleration, ρ_0 is a reference density, η_{EQ} is the equilibrium ocean tide height, η is the sea surface height, and $\langle \rangle$ denotes time averaging. Since $\eta \gg \eta_l$ (Shriver et al. 2012), we assume that $\eta \approx \eta_0$. The conversion and pressure fluxes are computed following Simmons et al. (2004a).

Unfortunately, it is not possible to cleanly separate the barotropic from the baroclinic dissipation because the wave and bottom drag terms depend quadratically and cubically on the velocity, respectively. We follow the ''linear'' separation technique by Kang and Fringer (2012). The total tidal velocities are separated in a barotropic and baroclinic component according to

$$(u, v) = (u_l + u_0, v_l + v_0), \tag{5}$$

where u and v are the velocities along the x (east–west) and y (north–south) axes. In the linear separation, we compute the barotropic and baroclinic time-mean dissipation due to bottom drag following

$$D_{b0} = \langle \rho_0 C_D |u_a| (u_a u_0 + v_a v_0) \rangle, \tag{6}$$

and

$$D_{bl} = \langle \rho_0 C_D |u_a|(u_a u_{la} + v_a v_{la})\rangle, \qquad (7)$$

where $C_D = 0.0025$ is the quadratic bottom drag coefficient, and subscript a indicates averaging over the bottom 10 m (as opposed to 500 m for the wave drag). All velocities within parentheses are bandpass filtered. The term $|u_a|$ is computed using the total unfiltered velocities. Note that the sum of D_{b0} and D_{bl} yields

$$D_b = \langle \rho_0 C_D |u_a|(u_a u_a + v_a v_a)\rangle. \qquad (8)$$

Similarly, the barotropic and baroclinic dissipation due to the linear wave drag reads

$$D_{w0} = \langle \rho_0 \mathbb{C}(u_a u_0 + v_a v_0)\rangle, \qquad (9)$$

and

$$D_{wl} = \langle \rho_0 \mathbb{C}(u_a u_{la} + v_a v_{la})\rangle, \qquad (10)$$

where $\mathbb{C}$ is the scalarized linear wave drag with units of meters per second, and subscript a indicates averaging over the bottom 500 m. Again, the sum of D_{w0} and D_{wl} yields

$$D_w = \langle \rho_0 \mathbb{C}(u_a u_a + v_a v_a)\rangle. \qquad (11)$$

In the appendix, we compare these terms with the "nonlinear separation" terms. An advantage of the linear separation is that it only yields two terms, that is, a barotropic and a baroclinic term for the bottom and wave drag, instead of an additional barotropic–baroclinic cross term as in the nonlinear separation. We find that the barotropic wave and bottom drag terms are similar in magnitude in both separations, whereas the differences between the baroclinic terms are within a factor of 2. In the nonlinear separation, both the spatial values and the global integral of the cross term are of the same order of magnitude as for the baroclinic term but generally negative. Because of this and the fact that the linear separation only has two terms, we use the linear separation in this paper. However, the reader should keep in mind (in particular for the baroclinic terms) that there is some adulteration by the barotropic flow.

3. Results

a. Integrated global balance

We present global integrals of the tidal-mean semidiurnal barotropic, baroclinic, and total energy balance terms in Fig. 1. The barotropic energy input in HYCOM of 3.12 TW compares well with the sum of the energy inputs to the semidiurnal constituents M_2, S_2, N_2, and K_2
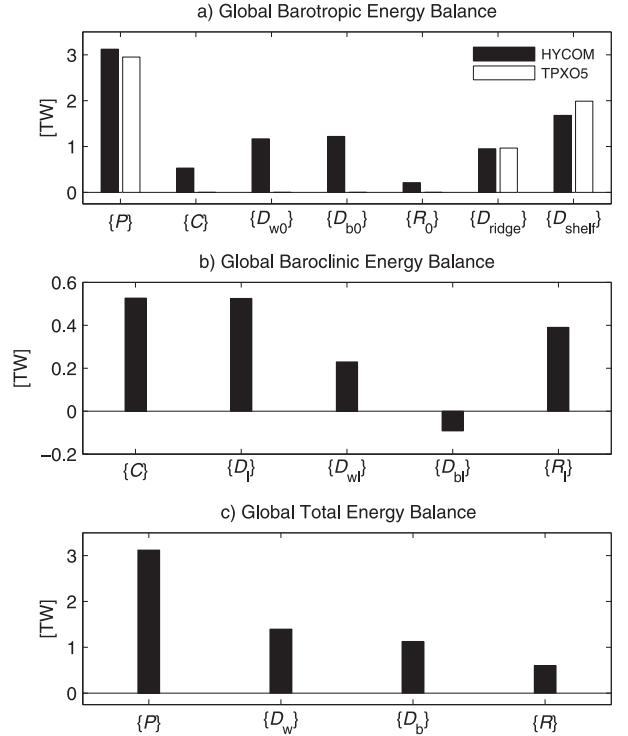

FIG. 1. Global semidiurnal (a) barotropic, (b) baroclinic, and (c) total energy balance. The barotropic dissipation rates $\{D_{\mathrm{ridge}}\}$ and $\{D_{\mathrm{shelf}}\}$ in (a) are computed for polygons encompassing mid-ocean ridges and shelf seas (Egbert and Ray 2001) and include contributions from C, D_{w0}, and D_{b0}.

of 2.95 TW in TPXO5, an altimetry-constrained barotropic tide model (Egbert and Ray 2003; Fig. 1a). The energy input of HYCOM is about 6% larger than the input of TPXO5. This slight overestimation may also affect the magnitude of the other energy terms, but we note that the uncertainty in these terms may also be due to other factors. For example, the uncertainty in the low-mode conversion is also caused by errors in the surface tide, stratification, and bathymetry. However, it is difficult to quantify these uncertainties. The energy conversion to the resolved low modes of $\{C\} = 0.53$ TW is about one-sixth of the energy input and about 50% of the energy loss to the barotropic wave drag $\{D_{w0}\} = 1.17$ TW, which represents the unresolved energy conversion to the high modes. Because high modes do not propagate as far as low modes, we assume that $\{D_{w0}\}$ also represents the high-mode dissipation. This means that about 30% of the total conversion $\{C + D_{w0}\}$ goes to the resolved low modes in this HYCOM simulation. In comparison, Simmons et al. (2004a) find $\{C\} = 0.89$ TW for M_2, but their water-level predictions are not as accurate as ours because of overly energetic barotropic tides.

Egbert and Ray (2001, 2003) computed the dissipation of barotropic energy for deep seas, areas including midocean ridges, and shallow seas, areas including shelves and shallow shelf seas. Egbert and Ray (2001) drew the boundaries of these areas well out into the deep ocean. Their deep and shallow seas include barotropic energy losses due to both internal tide conversion and bottom drag. We compute area-integrated dissipation rates $\{D_{\text{ridge}}\}$ and $\{D_{\text{shelf}}\}$ for these midocean ridge and shelf sea areas using the polygons of Egbert and Ray (2001, 2003). These polygons were digitized by Buijsman et al. (2015) from Fig. 2 of Egbert and Ray (2001). The terms $\{D_{\text{ridge}}\}$ and $\{D_{\text{shelf}}\}$ are integrals over C, D_{w0}, and D_{b0}. The polygons do not cover all midocean ridges. Hence, the integral over $\{D_{\text{ridge}}\}$ and $\{D_{\text{shelf}}\}$ of HYCOM is 0.3 TW smaller than the sum of $\{C\}$, $\{D_{w0}\}$, and $\{D_{b0}\}$. We compare $\{D_{\text{ridge}}\}$ and $\{D_{\text{shelf}}\}$ with the sum of the TPXO5 dissipation due to semidiurnal constituents for the deep and shallow seas (Table 1 of Egbert and Ray 2003). The agreement between HYCOM and TPXO5 in Fig. 1a appears to be quite good, suggesting that HYCOM correctly simulates the spatial distribution of the integral barotropic energy loss. The TPXO dissipation rates are computed from the difference between the barotropic energy input and flux divergence (Egbert and Ray 2001). These terms are one order of magnitude larger than the residual dissipation rate. As a consequence of this noisy process, the coastal areas have large positive and negative dissipation rates (Fig. 1 of Egbert and Ray 2003), suggesting that the uncertainty in the $\{D_{\text{shelf}}\}$ value of TPXO5 is larger than in $\{D_{\text{ridge}}\}$. In HYCOM, about 71% (1%) of $\{D_{\text{shelf}}\}$ ($\{D_{\text{ridge}}\}$) is due to bottom drag dissipation. We cannot compare the bottom drag dissipation in HYCOM with TPXO5 because TPXO only provides an integral estimate of the barotropic energy dissipation.

In the global, semidiurnal, baroclinic balance shown in Fig. 1b, the resolved barotropic to baroclinic conversion $\{C\}$ equals the low-mode dissipation $\{D_l\}$ because in the global integral the flux divergence equals zero. About half of this dissipation is due to the linear wave drag $\{D_{wl}\}$, while the other half may be attributed to viscous and numerical dissipation and uncertainties. As a result of the linear separation, the baroclinic dissipation due to bottom drag can be negative. This mainly occurs on the shelves, where the large total velocities are anticorrelated with the smaller baroclinic velocities.

In the total, global, semidiurnal balance shown in Fig. 1c, the dissipation due to wave drag is about equal to the dissipation due to bottom drag. The residual term, $\{\mathcal{R}\} = 0.60$ TW, is about 20% of the total energy input and may be attributed to viscous and numerical dissipation of the baroclinic waves and uncertainties in the energy term computations. In contrast, the barotropic residual $\{\mathcal{R}_0\} = 0.21$ TW and only constitutes 7% of the tidal energy input. We attribute this to the small role of viscous or numerical dissipation in the barotropic energy balance as compared to the baroclinic balance.

b. Spatial variability

In this section, we focus on the spatial variability of the barotropic dissipation, shown in Fig. 2, and the baroclinic energy terms, shown in Fig. 3. The barotropic dissipation due to the wave drag is spread over large horizontal scales, in particular at the midocean ridges (Fig. 2a). This is a consequence of limiting the wave drag to depths deeper than 500 m and to capping all peak values, which occur at the steepest and tallest ridges. This increases the drag strength of the deeper ridges relative to the taller ridges with capped values. This contrasts with the conversion shown in Fig. 3a, which is more concentrated at the steepest topographic slopes. As expected, the barotropic bottom drag is largest in coastal seas such as the European, Hudson, and Patagonia shelves (Fig. 2b). The baroclinic wave drag dissipation, shown in Fig. 2c, is weaker than the barotropic wave drag dissipation, consistent with the small abyssal signals of low baroclinic modes. Also, similar to the conversion, the baroclinic wave drag dissipation is more concentrated at the steepest topographic slopes, where the baroclinic velocities are large. The impact of quadratic bottom drag on the internal tides is small (Fig. 2d).

The barotropic to baroclinic conversion in HYCOM, shown in Fig. 3a, reflects the barotropic energy transfer to the low baroclinic modes, which is strongest at the steep and tall ridges in the Indian and Pacific Oceans. The conversion at the Mid-Atlantic Ridge is weaker because the ridge generates higher modes that are not well resolved in these simulations. Although mostly positive, the conversion can be negative when the local forcing is out of phase with remotely generated internal tides (Kelly and Nash 2010; Buijsman et al. 2010). The flux divergence, shown in Fig. 3b, is mostly positive at steep topography and negative away from topography. After subtracting the flux divergence from the conversion, the dissipation remains in Fig. 3c. The dissipation is positive in most locations, with the largest values at topography and smaller values in the abyssal ocean. The residual term, $\mathcal{R}_l = D_l - D_{wl} - D_{bl}$, shown in Fig. 3d, looks similar to D_l but is generally weaker. It represents the numerical and viscous dissipation and is largest close to topography where the wave generation is large.

The absolute semidiurnal fluxes, shown in Fig. 4, reveal the horizontal beam structure along which the internal tides propagate. The absolute fluxes provide a better indication of the internal tide generation sites
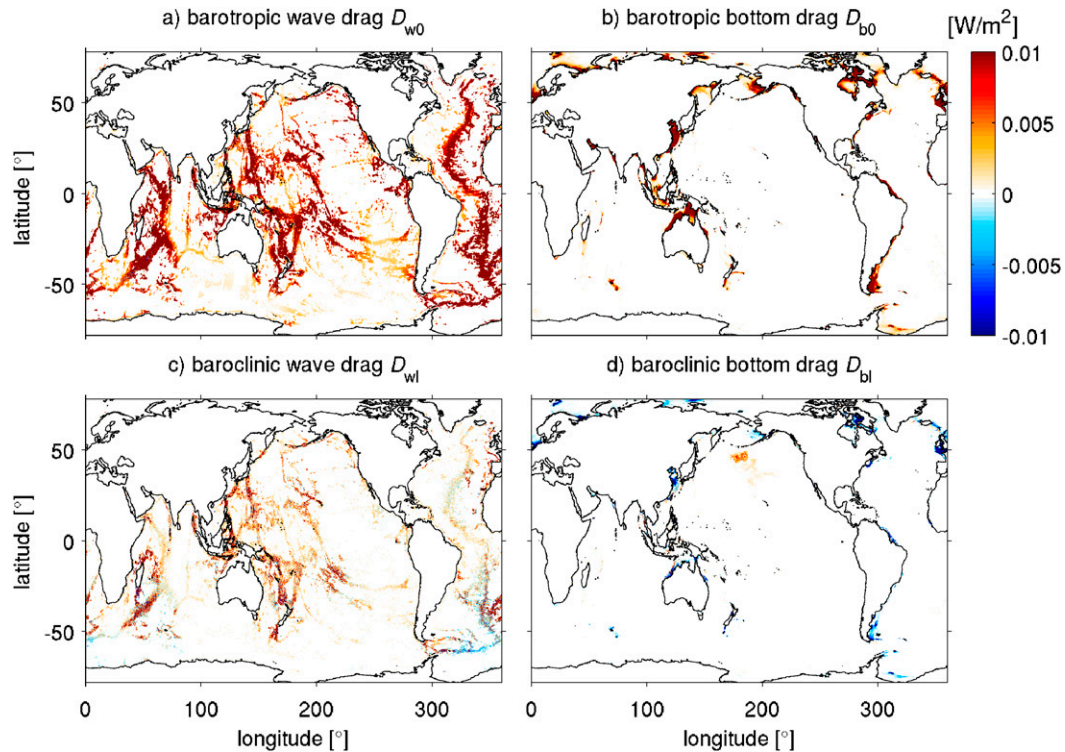
FIG. 2. Semidiurnal barotropic dissipation due to (a) linear wave drag and (b) bottom drag. Baroclinic dissipation due to (c) linear wave drag and (d) bottom drag.

than the conversion, for which large values at the steep and narrow ridges are barely visible. The fluxes in Fig. 4 reflect both the coherent and incoherent energy propagation. As a consequence, energy is seen propagating northward from the French Polynesian Islands in the South Pacific across the equator, a region with strong sheared mesoscale zonal flows.

The patches of positive bottom drag dissipation (Fig. 2d), positive and negative flux divergence (Fig. 3b), negative dissipation (Fig. 3c), positive residual dissipation (Fig. 3d), and fluxes (Fig. 4) south of the Aleutian Islands at ~45°N and north of Hawaii at ~37°N can most likely be attributed to unphysical thermobaric instabilities in HYCOM (Hallberg 2005). These instabilities occur in areas where the conversion is negligible (Fig. 3a) and are dissipated by bottom drag (Fig. 2d) and numerical and viscous dissipation (Fig. 3d). These instabilities have not been found outside the North Pacific Ocean. The approximate energy input into these waves is less than 2% of the global integral of the low-mode conversion.

c. Variability with seafloor depth

We compare conversion and dissipation terms, globally averaged over areas with ocean seafloor depths grouped in vertical increments of 250 m, in Fig. 5. This

provides insight into where the internal tides dissipate and into the mechanisms contributing to this dissipation. The area-averaged barotropic dissipation terms are the largest (Fig. 5b). The quadratic bottom drag mainly operates in water shallower than 250 m, whereas the wave drag operates in waters deeper than 500 m. In the global ocean, the barotropic wave drag dissipation peaks near 1000 m, while in the Atlantic Ocean it peaks near 3000 m due to the Mid-Atlantic Ridge (not shown).

Globally, the strength of the barotropic to baroclinic conversion $\{C\}$ in HYCOM is proportional to the barotropic wave drag dissipation $\{D_{w0}\}$, but the conversion is slightly smaller (Figs. 5b,c). The bulk of the low-mode internal tides are generated at tall ridges between 250 and 1500 m at topography that penetrates the thermocline (Simmons et al. 2004a). The baroclinic dissipation $\{D_l\}$ is larger than the flux divergence at all depths (Fig. 5c). Therefore, the fraction of conversion that is locally dissipated, $q = \{D_l\}/\{C\}$ (St. Laurent and Garrett 2002), is larger than 50% (blue line in Fig. 5e). In shallow waters of 250–500-m depth, near steep topography, about 60% of the locally generated, low-mode waves are dissipated (40% escapes), whereas at deeper topography more of the locally generated waves are dissipated. In water depths shallower than 250 m and in
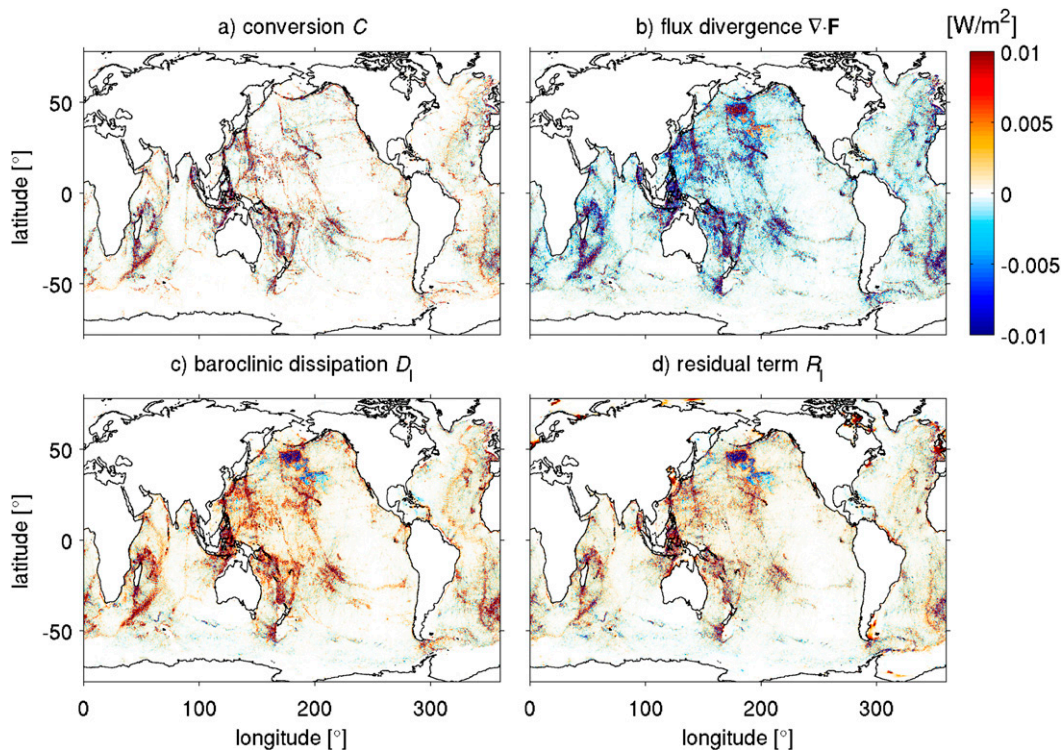
FIG. 3. The semidiurnal baroclinic energy balance with (a) the conversion, (b) the flux divergence, (c) the dissipation $D_l = C - \nabla \cdot \mathbf{F}$, and (d) the residual term $R_l = D - D_{wl} - D_{bl}$.

depths deeper than 3000 m, $q = 100\%$. About 73% of all the conversion at depths shallower than 3000 m is locally dissipated. In waters deeper than 3000 m, the flux divergence is negative in Fig. 5c: more internal tides are

dissipated than generated. This area covers about 75% of the global ocean (Fig. 5a).

The terms that compose the baroclinic dissipation are shown in Fig. 5d. In depths shallower than 1500 m, that
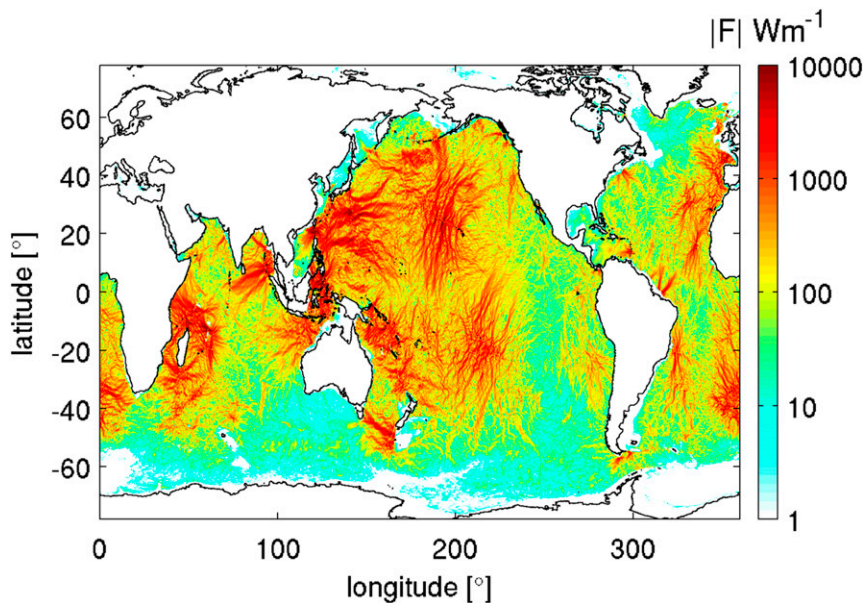

FIG. 4. The absolute semidiurnal baroclinic pressure fluxes reveal their beamlike structure. Note that the color scale is logarithmic.
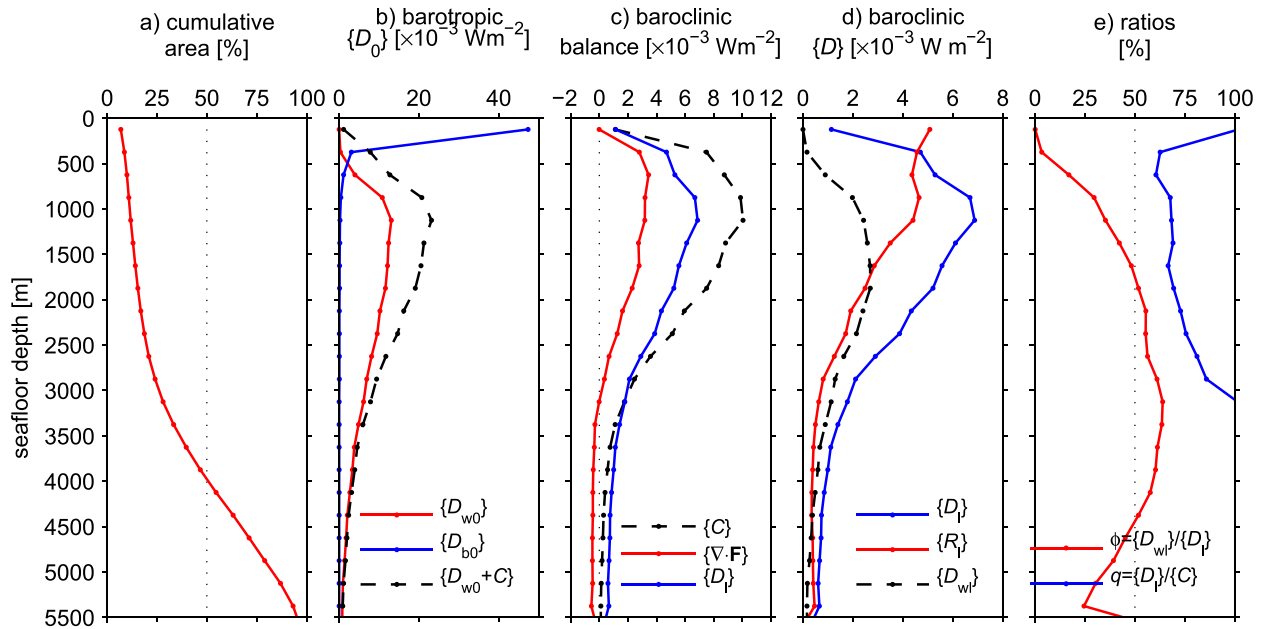
FIG. 5. Plotted as a function of seafloor depth are (a) the cumulative ocean floor area, (b) the barotropic dissipation terms, (c) terms of the baroclinic energy balance, (d) the baroclinic dissipation terms, and (e) the ratio between the baroclinic wave drag dissipation and the baroclinic low-mode dissipation and the fraction of the low-mode conversion that is locally dissipated. All values are averaged over depth bins of 250 m.

is, near steep topography, the baroclinic residual dissipation $\{\mathcal{R}_l\}$ is larger than the dissipation due to baroclinic wave drag $\{D_{wl}\}$ (Fig. 5d and red curve in Fig. 5e). Most likely, the large vertical shear in the horizontal velocities of the near-field waves causes large viscous and numerical dissipation. In intermediate depths of 1500–4500 m, covering about 50% of the global ocean, the dissipation due to baroclinic wave drag is larger than 50% of the total dissipation, that is, the wave drag plays a nonnegligible role in dissipating the internal tides. Finally, in water depths deeper than 4500 m, about 35% of the global ocean, viscous and numerical dissipation is larger than wave drag dissipation, which is small because of the absence of topography and strong currents.

d. Regional balance

We now consider the semidiurnal energy balance for two regions, shown in Fig. 6: the Luzon Strait, a well-known low-mode generation site with tall supercritical topography (e.g., Alford et al. 2011; Buijsman et al. 2014), and the south Mid-Atlantic Ridge (MAR), a deep, midocean spreading ridge with some supercritical slopes that generate higher modes (Zilberman et al. 2009). Supercritical topography has slopes that are steeper than the internal tide characteristics.

The Luzon Strait has two tall ridges that are perpendicular to the mixed diurnal–semidiurnal tide that propagates from the western Pacific Ocean to the South

China Sea (Fig. 6a). HYCOM predicts a low-mode energy conversion $\{C\}$ that is more than twice as large as the barotropic wave drag $\{D_{w0}\}$, that is, 70% of the conversion contributes to the low modes (Fig. 6b). About 70% (60%) of total (low mode) conversion is locally dissipated. In agreement with Figs. 5d and 5e in depths shallower than 1500 m, the dissipation due to wave drag $\{D_{wl}\}$ is smaller than the residual term, which represents dissipation due to unresolved breaking lee waves and strong vertical shear (Buijsman et al. 2012).

In contrast to Luzon Strait, the low-mode energy conversion at the deep MAR is much smaller than the barotropic wave drag dissipation, with $\{C\}$ being only 16% of the total low- and high-mode conversion. About 97% (82%) of the total (low mode) conversion is locally dissipated.

So far, our discussion on the modal representation in $\{C\}$ and $\{D_{w0}\}$ has not been very specific other than references to low and high modes. To remedy this, we compute the barotropic energy conversion to the first 10 baroclinic modes at the Luzon Strait and MAR (Fig. 7). As a first step, the HYCOM simulation output is regridded on z levels. Next, the semidiurnal M_2 complex harmonic constants are extracted with a least squares fit over 30 days. Using local, time-mean density profiles, the Stürm–Liouville equation is solved for the eigenfunctions of the vertical modes. The complex harmonic constants are fitted to the eigenfunctions.
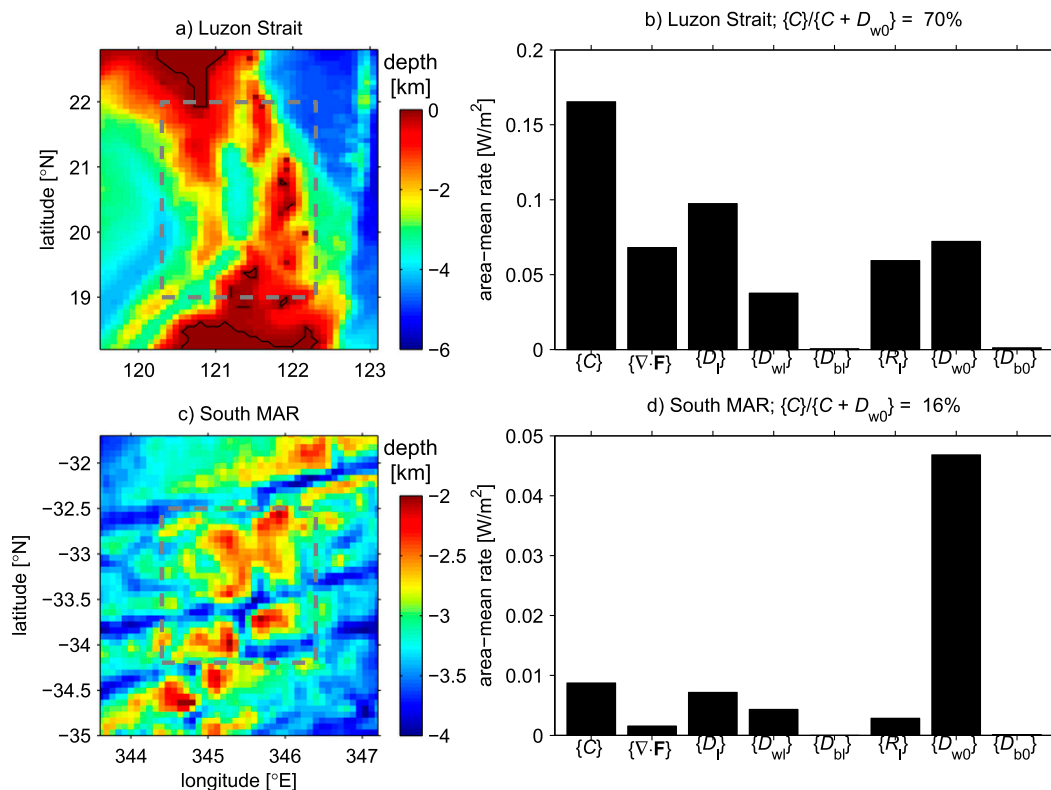
FIG. 6. Terms from the semidiurnal barotropic and baroclinic energy balances for (b) the Luzon Strait and (d) the south Mid-Atlantic Ridge. The dashed polygons in (a) and (c) mark the areas for which the energy terms are computed against a background of seafloor depth.

Finally, the barotropic to baroclinic mode conversion is computed. The above analysis is explained in detail in Buijsman et al. (2014) and references cited therein.

At Luzon Strait (Fig. 7a), the HYCOM conversion rates are compared with conversion rates computed using MITgcm simulations with tidal forcing only, 50 z layers, and 2-km horizontal resolution (Buijsman et al. 2014). The MITgcm simulations should resolve at least the first 10 modes. The M_2 MITgcm conversion rates are computed during a spring–neap cycle, and S_2 is aliased into these rates. To compare with the HYCOM M_2 rates, the MITgcm rate is scaled by the squared ratio of the M_2 to spring tide barotropic velocity amplitudes (0.77^2; Buijsman et al. 2014). HYCOM and MITgcm show a relatively good agreement in magnitudes for modes 1 and 2, but the higher modes drop off more rapidly in HYCOM than in MITgcm. The area-averaged conversion rate summed over all 10 modes in HYCOM and MITgcm are 0.11 and 0.14 W m^{-2}, respectively.

At the MAR (Fig. 7b), we compare the HYCOM dissipation rates with conversion rates computed from the Princeton Ocean Model (POM) by Zilberman et al. (2009). The POM simulations feature a 750-m horizontal resolution and 61 vertical sigma levels. The HYCOM

versus POM comparison is fairly good for modes 1–3. In both models, mode 2 is predicted to be the most dominant, consistent with the dominant length scales of the topographic slope spectrum (Zilberman et al. 2009). Although not shown, the POM conversion drops off quickly beyond mode 10 and has decreased to 1.5×10^{-4} W m^{-2} by mode 20. At the MAR, HYCOM does not resolve the conversion to modes 3 and higher as compared to the high-resolution POM. The area-averaged conversion rate summed over all 10 modes in HYCOM and POM are 0.006 and 0.01 W m^{-2}, respectively.

A question that arises is whether the lack of high-mode conversion in $1/12.5°$ HYCOM is correctly accounted for with the barotropic wave drag $\{D_{w0}\}$. Judging from the Luzon Strait and MAR cases, it appears that the cutoff to properly resolve modes in $1/12.5°$ HYCOM lies between modes 3 and 4. For the MAR, the unresolved high-mode conversion for M_2 tides in $1/12.5°$ HYCOM is about 7 (4) times larger than the conversion to modes 4–10 (4–20) in POM. For Luzon Strait, the unresolved high-mode conversion for M_2 tides in HYCOM is about 3 times larger than the conversion to modes 4–10 in MITgcm.
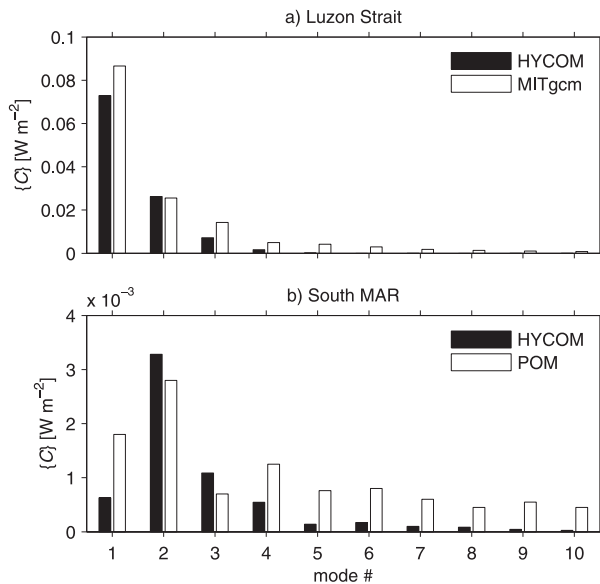
FIG. 7. M_2 barotropic energy conversion to the first 10 baroclinic modes for (a) HYCOM and 2-km MITgcm (Buijsman et al. 2014) at Luzon Strait and (b) HYCOM and 0.75-km POM at the south Mid-Atlantic Ridge. The POM values are taken from Fig. 8 of Zilberman et al. (2009).

In summary, 1/12.5° HYCOM does not satisfactorily resolve the energy conversion beyond modes 2 or 3 due to its relatively course grid size of about 8 km. This is less of an issue in Luzon Strait, where the tall topography, reasonably well resolved by the 8-km resolution and the strong tidal forcing are conducive to mode-1 and mode-2 wave generation. In contrast, at the deeper MAR, with a weaker forcing and smaller-scale topography, higher modes become relatively more important. While the ratios of the low-mode conversion to the high-mode conversion for HYCOM and the high-resolution models show the same trends, that is, they are >1 and <1 at Luzon Strait and the MAR, respectively, the magnitude of the barotropic wave drag dissipation in HYCOM is still too large compared to the high-mode conversion in the high-resolution models.

e. Fate of the internal tides

As the internal tides propagate away from their sources, their decay is in part affected by the strength of the internal wave drag, which can be considered a parameterization of high-mode scattering. If HYCOM can correctly predict this decay, we may utilize HYCOM to address how much of the internal tide energy reaches the continental shelves. In this section, we compare the depth-averaged dissipation rates in HYCOM with rates extracted from Argo float profiles by Whalen et al. (2012, 2015) and with rates inferred from the internal tide energy fluxes and amplitudes computed from altimetry-observed sea surface heights (SSH) by Zhao et al. (2010, 2012). Although neither of these comparison datasets is perfect, their combined usage provides more insight into the HYCOM strengths and limitations than each dataset would on its own.

1) GLOBAL COMPARISON

The Argo-inferred dissipation rates are compared with semidiurnal bandpassed HYCOM dissipation rates in Table 1 and Fig. 8. The drawback of using Argo float dissipation rates is that they represent dissipation from many types of flows—dissipation over all tidal constituents and due to near-inertial waves—at the same time that they provide limited horizontal and vertical coverage. The HYCOM dissipation rates in this paper are associated with semidiurnal tides only. The diurnal tidal energy input is about 1/5 of the semidiurnal energy input. The exclusion of nontidal dissipation sources and diurnal tides, as a consequence of the bandpass filtering of HYCOM data, suggest the Argo dissipation rates will be larger. A quantitative comparison is further complicated because Argo data are absent below depths of 2000 m. Hence, we minimize a quantitative comparison (Table 1) and emphasize the comparison of the spatial patterns in the Argo and HYCOM dissipation rates (Fig. 8).

Whalen et al. (2012, 2015) computed dissipation rates based on strain information from Argo float profiles below the mixed layer and in the upper 2000 m of the ocean. They averaged the data to horizontal cells of 1.5° and three layers bounded by 250 and 500 m, 500 and 1000 m, and 1000 and 2000 m. We only use cells if they contain at least three dissipation rate estimates. The lack of Argo data below 2000 m limits an accurate comparison with the HYCOM dissipation rates, which are

TABLE 1. Global comparison of Argo-inferred and HYCOM, area-averaged, depth-mean dissipation rates for areas with seafloor depths shallower and deeper than 4000 m. The lower- and upper-bound dissipation rates, Argo$_{low}$ and Argo$_{high}$, are defined in the text. HYCOM$_l$ and HYCOM$_{l+w0}$ refer to the resolved low mode and the sum of the resolved low-mode and baroclinic wave drag dissipation rates. The last column indicates the percentage of ocean area covered with gridded Argo data.

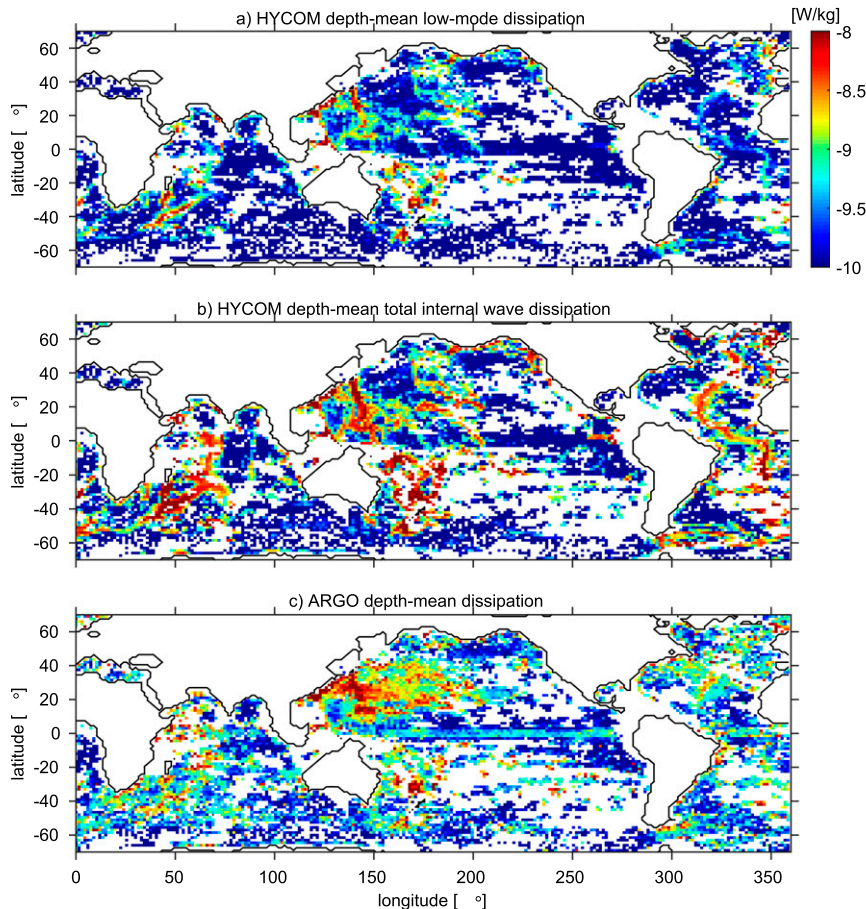| Seafloor depth	$\{\epsilon\} \times 10^{-9}$ (W kg^{-1})				Argo area coverage (%)
	Argo$_{low}$	Argo$_{high}$	HYCOM$_l$	HYCOM$_{l+w0}$	
<4000 m	0.61	2.14	1.02	3.38	50
>4000 m	0.13	0.96	0.15	0.50	67

FIG. 8. Depth-mean dissipation rates (a) ϵ_l of HYCOM, (b) $\epsilon_l + \epsilon_{w0}$ of HYCOM, both for the semidiurnal band, and (c) based on Argo floats (Whalen et al. 2015). All grid cells with Argo values have incomplete coverage in the vertical. The dissipation rates shown are the layer-averaged values. They can be considered upper-bound estimates. Only grid cells are shown that have both HYCOM and Argo data.

inferred from the depth-integrated energy balance. In this paper, we do not make a comparison of HYCOM and Argo dissipation rates as a function of depth. This is because HYCOM lacks sufficient realism in the vertical due to, for example, coarse (bottom) layers with thicknesses of $O(100)$ m and the inability to resolve high vertical modes and their dissipation. Instead we compute depth-mean Argo dissipation rates using two methods, yielding lower- and upper-bound estimates that can be compared with HYCOM dissipation rates. As a lower-bound estimate, we vertically integrate all Argo values over their layers in each 1.5° cell and then normalize them by the seafloor depth. As an upper-bound estimate, we assume that the dissipation rates averaged over the three layers with Argo data represent the depth-mean dissipation rate. This upper-bound estimate most likely causes larger deviations from the actual dissipation rates for deep as compared to shallow

areas. Areas with seafloor depths deeper than 3000–4000 m generally feature smoother topography. In these areas the Argo dissipation rates generally decline with depth (results not shown).

The Argo-based dissipation rates comprise the high-mode internal tide breaking at generation sites and the low-mode breaking and scattering in the far field. Hence, the Argo dissipation rates should be compared with the sum of the resolved low-mode dissipation D_l and the unresolved high-mode conversion and immediate dissipation D_{w0}. We compute depth and area-mean values for the same grid used for the Argo dissipation rates according to $\{\epsilon_l\} = \{D_l\}/(\rho_0\{H\})$ and $\{\epsilon_{w0}\} = \{D_{w0}\}/(\rho_0\{H\})$, where ρ_0 is a reference density, and H is seafloor depth.

The area- and depth-mean dissipation rates inferred from Argo and HYCOM are shown in Table 1. The dissipation rates are computed for areas with seafloor

depths shallower and deeper than 4000 m. About 50% of the ocean is shallower than this depth (Fig. 5). In shallow water the low-mode HYCOM dissipation rates fall in between the lower- and upper-bound Argo dissipation rates, while the sum of the resolved low-mode and parameterized high-mode dissipation is about 1.6 times larger than the upper-bound Argo estimates. This confirms our previous findings that the barotropic dissipation associated with the wave drag may be too strong. The HYCOM and Argo dissipation rates are a factor of 2–4 smaller in areas where the seafloor depths are larger than 4000 m (Table 1). For these areas, the HYCOM dissipation rates fall in between the Argo lower- and upper-bound dissipation rates. However, the upper-bound Argo dissipation rate may overestimate the dissipation for areas with large water depths because in deep areas the dissipation rates generally decline with depth.

The Argo dissipation rates contain more sources of dissipation than just the internal tide. If we omit areas with high eddy kinetic energy (EKE $> 0.05 \, \mathrm{m^2 \, s^{-2}}$), as computed by Whalen et al. (2012), and near-inertial energy input between $|30°|$ and $|40°|$ latitude, the shallow-water (deep-water) Argo and HYCOM dissipation rates are reduced on average by 22% and 16% (12% and 7%), respectively, not significantly improving our comparison.

We find that the Argo dissipation rates in both shallow and deep water are generally larger over rough than smooth topography (see also Whalen et al. 2012). This implies that, even for areas with large seafloor depths (>4000 m), the dissipation due to breaking internal waves penetrates the upper water column where it can be recorded by the Argo floats. In addition to using the Argo dissipation rates to mark the possible upper and lower bounds of dissipation, we can also use the Argo data for a spatial comparison with the HYCOM data. The spatial patterns for the depth-mean dissipation rates of HYCOM (ϵ_l and $\epsilon_l + \epsilon_{w0}$), and for the upper-bound dissipation estimates for the Argo data, are displayed in Fig. 8. In most areas with topography, the HYCOM dissipation due to only low-mode waves (Fig. 8a) is lower than the Argo-inferred dissipation (Fig. 8c). Upon adding the unresolved high-mode generation and dissipation ϵ_{w0} to ϵ_l (Fig. 8b), we see that the dissipation at the midocean spreading ridges in the Atlantic and Indian Ocean is significantly enhanced compared to Argo-based dissipation rates in Fig. 8c. Nevertheless, the agreement is striking, with the largest dissipation occurring over rough topography in all subplots. Also, note the absence of dissipation away from generation sites in both HYCOM and Argo, for example, in the eastern Pacific and northeastern Indian Oceans.

In summary, while the spatial patterns of HYCOM and Argo-inferred depth-mean dissipation rates reveal many similarities and while the low-mode internal tide dissipation rates fall within the upper and lower bounds inferred from Argo floats, the limited spatial coverage of the Argo floats and the multiple dissipation sources that may affect the Argo dissipation rates prevent us from drawing firmer conclusions.

2) DECAY OF INTERNAL TIDES ALONG A BEAM

In the previous section, we presented global integrals of internal tide dissipation. In this section, we consider the decay of low-mode internal tides along horizontal beams radiating southward and northward from the French Polynesian Islands in the tropical South Pacific (Fig. 9), a region that has received less attention than Hawaii. As with Hawaii, these volcanic French Polynesian Islands rise steeply from the ocean seafloor and are oriented along long ridges. HYCOM predicts M_2 tidal elevations of ~30 cm and RMS errors with TPXO7.2 of about ~3 cm (Shriver et al. 2012). We choose this region because the islands generate strong semidiurnal internal tides whose propagation is not affected by remotely generated waves as much as the propagation of the Hawaiian waves is. Thus, we can study the decay of unidirectional wave beams from one line source more cleanly around the French Polynesian Islands than around Hawaii.

Following the plane-wave fit method of Zhao et al. (2010, 2012), we compute SSH mode-one M_2 amplitudes and SSH-derived mode-1 M_2 energy fluxes for northward- and southward-propagating internal tides using up to 20 yr of satellite altimetry from TOPEX/ Poseidon (TP)–Jason, TP–Jason tandem, European Remote Sensing (ERS) satellites, and *Geosat Follow-On* (*GFO*), and 3 yr of HYCOM SSH time series (Shriver et al. 2012). Ansong et al. (2015) showed that the amplitude of the coherent tide equilibrates for time series longer than about 3 yr. Hence, we assume that both our results derived from altimeter and HYCOM SSH output represent equilibrated values, making it reasonable to compare them. The fluxes are shown in Fig. 9. The northward and southward SSH-derived fluxes generally agree in magnitude and direction between altimetry and HYCOM, but there is some disagreement in the details. For example, the strong northward beam in the altimetry near 20°S and 225°E (Fig. 9a) is barely visible in HYCOM (Fig. 9c). These differences between the HYCOM simulations and altimetry may be due to inaccuracies in HYCOM's surface tides, topography, stratification, and/or model setup. As a result of the plane-wave fit method, the SSH-derived fluxes have a more diffuse appearance and a smaller amplitude than
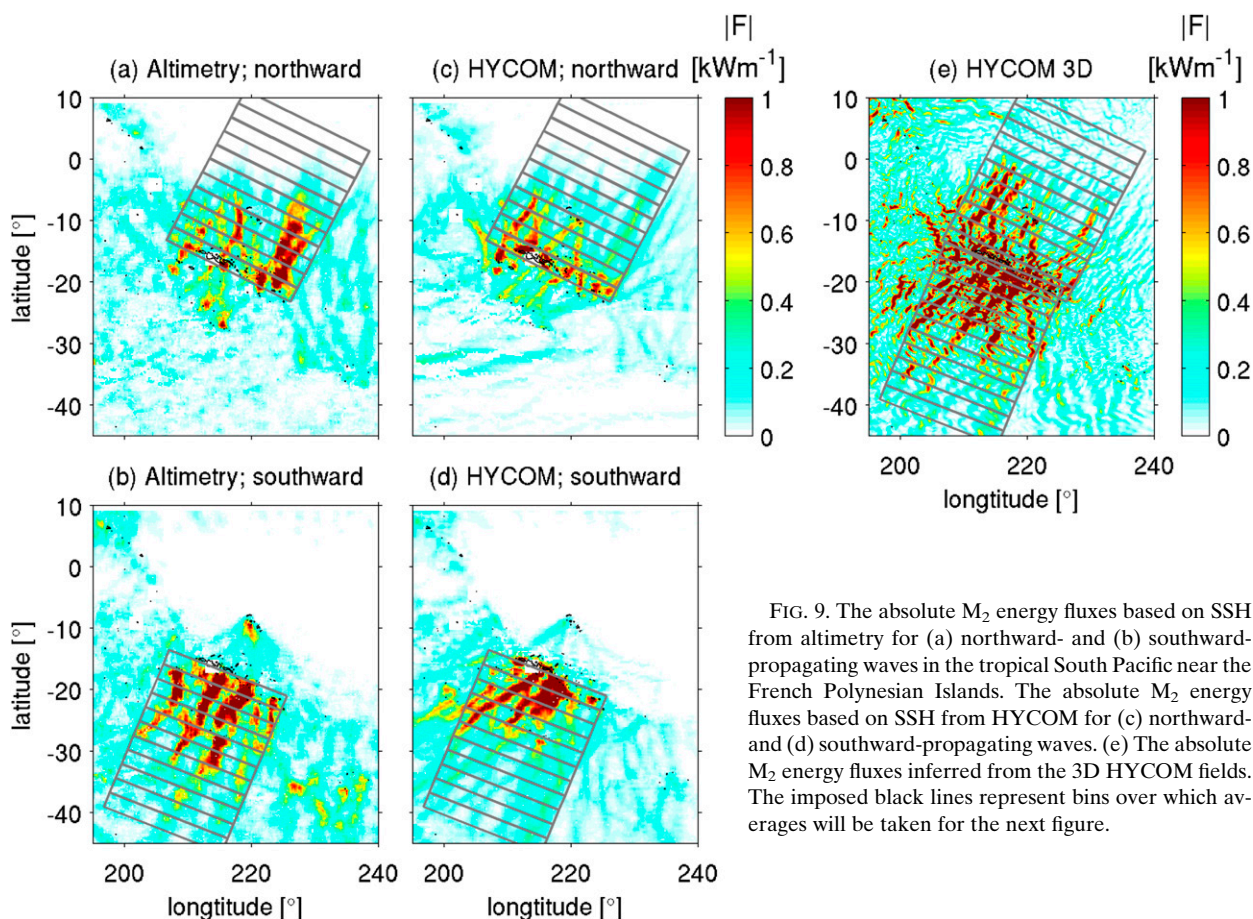
FIG. 9. The absolute M_2 energy fluxes based on SSH from altimetry for (a) northward- and (b) southward-propagating waves in the tropical South Pacific near the French Polynesian Islands. The absolute M_2 energy fluxes based on SSH from HYCOM for (c) northward- and (d) southward-propagating waves. (e) The absolute M_2 energy fluxes inferred from the 3D HYCOM fields. The imposed black lines represent bins over which averages will be taken for the next figure.

the M_2 fluxes computed from the 30-day time series of 3D HYCOM fields (Fig. 9e).

We area average the M_2 SSH amplitudes over 11 bins on both sides of the islands (Fig. 9). The results in Figs. 10c and 10d reveal a reasonable agreement between HYCOM and the altimetry, in particular on the south side. The altimetry SSH amplitudes are generally larger by 5%, but they seem to decay faster north of the islands near $-5°$. This decay is not necessarily attributed to energy loss but most likely to the strong mesoscale activity at the equator, which decouples the phase of the internal tides from the phase at the generation site. The duration of the time series applied to the least squares fit method inversely affects the magnitude of the coherent amplitude captured (Shriver et al. 2014). Hence, the amplitudes in the longer altimetry time series decay faster when strong mesoscale eddies are present.

The bin-averaged M_2 SSH-derived fluxes in Figs. 10e and 10f feature the same trends as for the SSH amplitudes, but the fluxes inferred from altimetry are about a factor of 1.17 larger than the HYCOM fluxes. This factor is larger than for the SSH amplitudes (1.05) because the fluxes scale with the amplitude squared. The M_2 fluxes

computed from the 3D HYCOM fields (red dashed curve) are on average 1.5 larger than the HYCOM SSH-derived fluxes. Reasons for this are attributed to, for example, the longer time series leading to smaller coherent amplitudes and the plane-wave fit method, which creates smoother fields. For comparison, we also show the semidiurnal bandpassed fluxes in black in Figs. 10e and 10f. Compared to the harmonically derived M_2 fluxes, the bandpassed fluxes reflect both the coherent and incoherent waves. These fluxes are minimally affected by the mesoscale activity at the equator. South of the Polynesian Islands, this activity is not present, and both the bandpassed and M_2-fitted signals show a more congruous decay.

Next, we compute bin- and depth-averaged dissipation rates from the divergence of the SSH-derived and 3D HYCOM M_2 fluxes (red solid, red dashed, and blue curves in Figs. 10g,h). These dissipation rates are of the same order of magnitude and decline away from the Polynesian Islands. We compare these rates with the semidiurnal bandpassed HYCOM estimates of ϵ_l (lower bound) and $\epsilon_l + \epsilon_{w0}$ (upper bound of the black envelope) and with the Argo lower- and higher-bound estimates
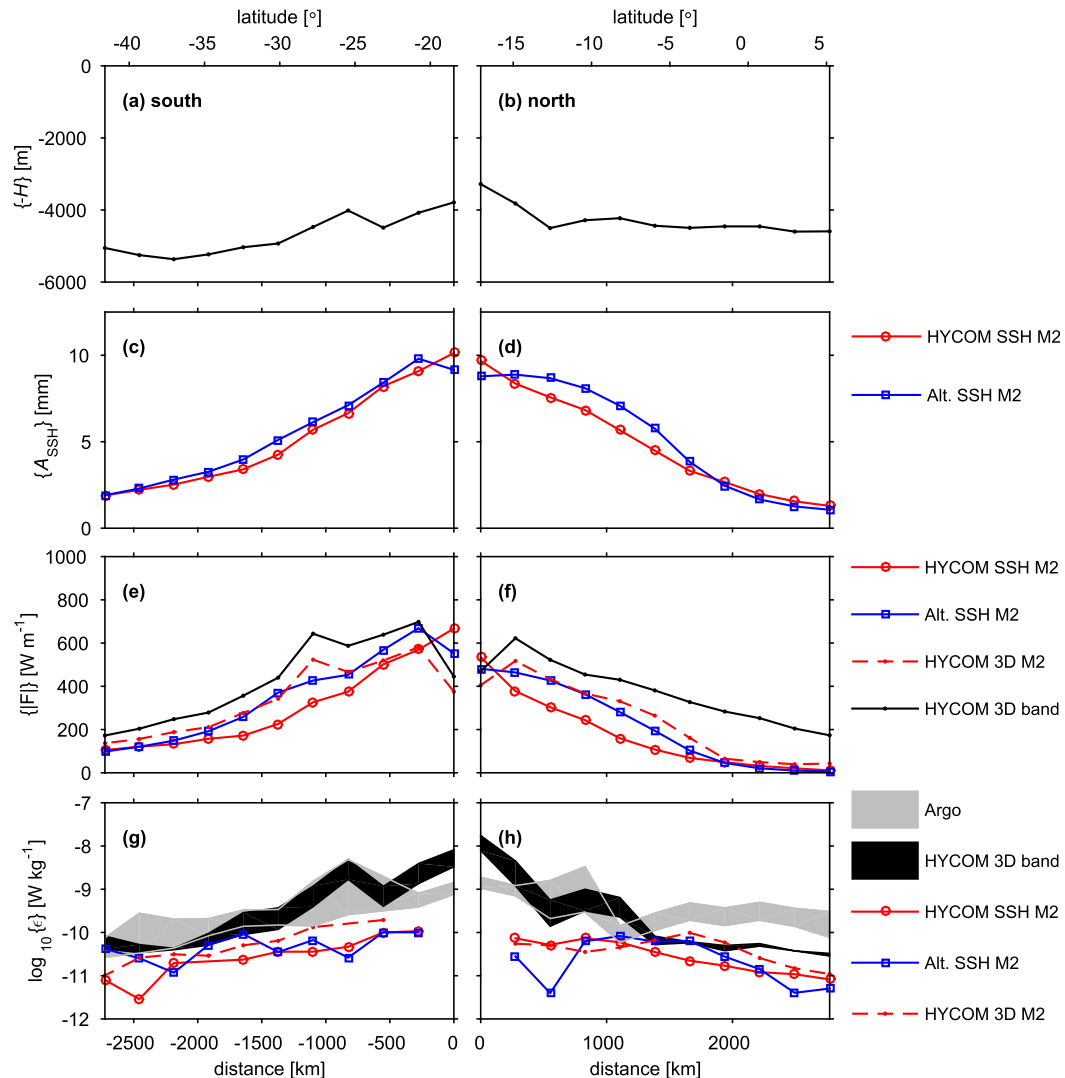
FIG. 10. Decay of semidiurnal internal tides to the south and north, away from the French Polynesian Islands; the bathymetry (a) to the south of the islands and (b) to the north, the (c),(d) SSH amplitudes, the (e),(f) absolute fluxes, and the (g),(h) dissipation rates. Altimetry is abbreviated with Alt. The SSH amplitudes and SSH-inferred fluxes and dissipation rates are computed for mode-one M_2 waves. Variables labeled HYCOM 3D band (HYCOM 3D M_2) are computed using semidiurnal bandpassed (M_2) 3D HYCOM fields. The dissipation rates labeled with SSH and HYCOM 3D M_2 in (g) and (h) are computed from the flux divergence only. The envelopes for the bandpassed HYCOM dissipation rates in black are bounded by the low-mode and total dissipation rates. The Argo dissipation rates in gray are bounded by the lower- and upper-bound estimates. All values are averaged over bins that are shown in Fig. 9.

(the gray envelope). The Argo and bandpassed rates are generally higher than the rates inferred from flux divergence because these latter rates are computed without the contributions of conversion and high-mode dissipation at topography, for example, at −25°, −18°, and −10°. The incoherence of the M_2 internal tide increases the apparent dissipation near −5° (red dashed and blue curves in Fig. 10h) compared to the dissipation of the semidiurnal bandpassed internal tide (black envelope).

The HYCOM semidiurnal bandpassed dissipation rates agree with the Argo dissipation rates for the majority of this region (Figs. 8g,h). Both rates are elevated at the small ridges at −25° and −10°. The Argo dissipation rates are potentially biased by the limited coverage in this area. One discrepancy is within 300 km of the islands where the HYCOM dissipation rates are significantly higher than the Argo dissipation rates. The elevated Argo dissipation rates along the equator north of −5° may be due to contamination from noninternal

TABLE 2. The semidiurnal, bandpassed, low-mode conversion, flux divergence, and dissipation for coastal regions shallower than ~4 km, as shown in Fig. 11. A positive divergence indicates a net flux out of the coastal region.

Ocean	$\{C\}$ (GW)	$\{\nabla \cdot \mathbf{F}\}$ (GW)	$\{D\}$ (GW)	$\{D\}/\{C\}$ (%)
Pacific	45.0	1.1	43.8	97
Atlantic	18.7	0.5	18.2	98
Indian	31.6	−0.7	32.3	102
Total	95.2	0.9	94.3	99

wave strain at the equator (i.e., equatorial deep jets), due to deviations from the Garrett–Munk internal wave spectrum used in the finescale parameterization at the equator (Whalen et al. 2015), or due to internal waves interacting with equatorial processes in ways not well represented in HYCOM.

In summary, HYCOM internal tide SSH amplitudes and SSH-derived fluxes compare well in magnitude and trends with altimetry-derived values when some regional averaging is performed. The altimetry-derived SSH amplitudes and fluxes are on average 1.05 and 1.17 times larger than the HYCOM equivalents, respectively. As the harmonic fitting techniques map phase incoherence to nonexisting internal tide dissipation, this comparison is not ideal, but at least it shows that the combination of internal tide dissipation and the effect of eddies on internal tide phases is reasonably well represented in HYCOM.

3) ARE THE CONTINENTAL MARGINS SINKS?

Internal tides reaching the continental margins may reflect, scatter, and dissipate on the (super)critical part of the shelf slope or propagate onto the shelf (Kelly et al. 2013). We compute energy balances for these coastal regions and landward fluxes into these regions for the semidiurnal bandpassed internal tides for the three largest ocean basins (Tables 2, 3). The coastal regions contain the shelf, the steepest part of the shelf slope, and in some cases part of the abyssal plain. These regions are indicated with colored polygons in Fig. 11. Ideally, the seaward boundary of these polygons should have been

the toe of the shelf slope, but in general, this boundary is located farther seaward in depths varying between 2000 and 4000 m. The location of the boundary is determined by the landward extent of the grid of the plane-wave fitting technique, discussed below, a procedure that works best in deep water away from steep shelf slopes and coastal boundaries. We assume that this seaward shift in boundaries has a minimal impact on the magnitude of the fluxes that reach the shelf slope and shelf where they may dissipate. The flux divergence integrated over the coastal regions in the Pacific and Atlantic Oceans in Table 2 is positive, reflecting a net energy flux out of the coastal regions. This can be attributed to strong shelf sources such as from the Indonesian Archipelago, the Kuroshio region, and the Aleutian Islands in the Pacific and the Amazon shelf and the Bay of Biscay in the Atlantic. Only the coastal regions in the Indian Ocean receive a net flux of energy from deep water, which may be attributed to the strong deep-water sources around Madagascar. Compared to the local, low-mode conversion in the coastal regions, the net energy fluxes are small. Hence, most of the locally generated energy is locally dissipated (Table 2). The global integral of the shelf conversion is 95.2 GW, which is about 27% of total conversion of 348.7 GW in the abyssal oceans seaward of the continental margins (Table 3). Thus, the continental margins cannot be ignored as a source. The sum of the abyssal and shelf conversion of 444 GW is 84% of the global integral of 526 GW. The exclusion of the sources within the Indonesian Archipelago largely explains this difference.

We compute the landward fluxes into the coastal polygons in two different ways (Table 3). The term $\{F_{3D}\}$ is computed from the semidiurnal, bandpassed, 3D HYCOM fields. At each model grid point, this flux represents the sum of all wave energy. We only count the fluxes that are directed into the coastal regions. Hence, $\{F_{3D}\}$ represents a lower-bound estimate. To better separate the landward from the seaward fluxes, we employ the plane-wave fitting method of Zhao et al. (2010, 2012) for M_2 SSH for the 30-day HYCOM time series. The landward fluxes $\{F_{plane}\}$ are computed by

TABLE 3. Deep-water conversion and landward fluxes for the semidiurnal bandpassed fields; $\{F_{3D}\}$ is computed from the 3D model fields and represents the landward flux that is directed into the polygons; $\{F_{plane}\}$ is computed by separating three mode-1 wave fields using the plane-wave fitting method for M_2 SSH. The wave fluxes directed into the coastal polygons are summed and scaled to match semidiurnal low-mode bandpassed estimates.

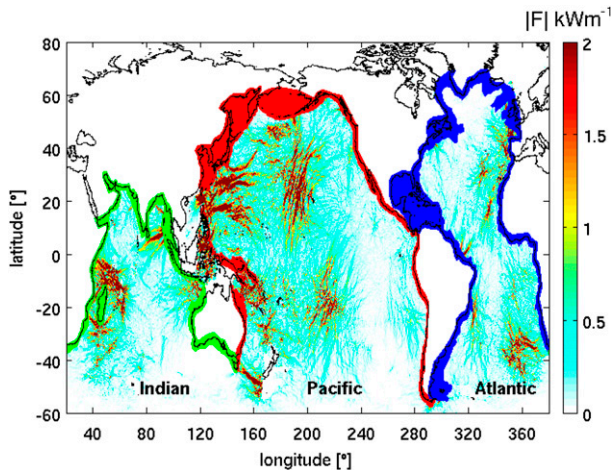| Ocean	$\{C\}$ (GW)	$\{F_{3D}\}$ (GW)	$\{F_{3D}\}/\{C\}$ (%)	$\{F_{plane}\}$ (GW)	$\{F_{plane}\}/\{C\}$ (%)
Pacific	198.0	9.0	4.6	17.5	8.8
Atlantic	70.3	4.4	6.3	13.5	19.2
Indian	80.4	6.8	8.4	12.3	15.3
Total	348.7	20.2	5.8	43.3	12.4

FIG. 11. Semidiurnal, bandpassed, low-mode energy fluxes and colored polygons marking the coastal regions including the shelf and shelf slope in the Indian Ocean (green), Pacific Ocean (red), and Atlantic Ocean (blue). In the ocean, the polygons are approximately located between the 2- and 4-km isobaths.

separating three M_2, mode-1 wave fields; summing the fluxes directed into the coastal polygons; and scaling them by a factor of about 1.3 to match semidiurnal bandpassed estimates to correct for incoherence and other semidiurnal constituents. As expected, $\{F_{3D}\}$ is roughly half of $\{F_{plane}\}$. Globally, about 12% of the deep-water internal tide energy propagates into the coastal regions (Table 3). The continental margins of the Pacific Ocean receive the least amount of energy from the deep-water sites (9%) because these sites are, on average, located farthest away from the margins, while the coastal regions of the Atlantic Ocean receive the most (19%).

4. Discussion and conclusions

In this paper, we have for the first time diagnosed global and regional semidiurnal barotropic and baroclinic energy balances in global HYCOM, a model forced by both atmospheric fields and the astronomical tidal potential. Using a linear split similar to Kang and Fringer (2012), we consider the energy losses to linear wave and quadratic bottom drag in the barotropic and baroclinic energy balances. We find a reasonable agreement between HYCOM on the one hand and TPXO, Argo data, altimetry data, and regional models on the other. The insights obtained in this analysis may be of use for future global ocean model simulations.

a. Low- versus high-mode conversion

HYCOM utilizes the linear wave drag scheme of Garner (2005). The wave drag is applied to the tidal velocities in the bottom 500 m, such that it damps both surface and internal tides. As in Arbic et al. (2004, 2010), we argue that the wave drag represents the energy conversion and subsequent dissipation of unresolved high modes. We find that HYCOM overestimates the barotropic energy loss to the wave drag scheme compared to regional high-resolution models and Argo-inferred dissipation rates.

Comparisons of HYCOM with regional high-resolution model studies of the steep ridges of Luzon Strait and the deep Mid-Atlantic Ridge demonstrate that 1/12.5° HYCOM does not adequately resolve the energy conversion to mode 3 and higher. This inability is more important at deeper and flatter ridges such as the MAR. Compared to the regional model of Zilberman et al. (2009), 1/12.5° HYCOM predicts about 40% less energy conversion to modes 1 to 10 at the MAR, most of which is in modes 4–10. In principle, this under-prediction should be compensated for with a linear wave drag scheme that only accounts for the energy conversion to high modes, such as the scheme of Falahat et al. (2014). However, the Garner (2005) scheme, which applies to the complete mode spectrum, was crudely modified 1) to yield a reasonable surface tide prediction and 2) to avoid spurious residual circulations (Arbic et al. 2010). For this purpose, the drag strength was reduced to zero for grid points with seafloor depths shallower than 500 m and was limited to a minimum e-folding time scale elsewhere. Although this places relatively more drag into deeper water, where high-mode generation is more important, the scheme overestimates the high-mode dissipation. Compared to the regional models, HYCOM overestimates the energy conversion to modes 4–10 by a factor of 7 and 3 for the MAR and Luzon Strait, respectively.

In the HYCOM simulations about 31% of the total conversion is due to the energy conversion to modes 1–3. Using their wave drag scheme, Falahat et al. (2014) computed an M_2 energy conversion to the first (two) three modes that is (58%) 72% of the conversion to the first 10 modes. However, the low-mode to total conversion ratio of HYCOM is likely a lower-bound estimate because HYCOM possibly overestimates the barotropic energy loss to the wave drag.

There are several reasons why the wave drag term in HYCOM may be too large. Its main purpose has been to improve the surface tide prediction, while it has not been tuned to correctly represent the internal tide energetics. The wave drag strength is tuned with an amplification factor. An incorrect representation of bathymetry and coastal geometry may adversely affect the tidal water–level predictions (Egbert et al. 2004). These predictions can be improved by applying an amplification factor that

is larger than the case in which coastal geometry does not adversely affect the predictions (Buijsman et al. 2015). Moreover, the application of a wave drag in HYCOM that is made to represent the full wave spectrum may not be correct in a model that resolves the low modes. Ideally, a wave drag should be used that only represents the high modes. However, the grid size and accuracy of the bathymetry should dictate what modes should be represented by such a scheme.

b. Internal tide dissipation

In water shallower than 2000 m, near the wave generation sites (steep ridges) or dissipation sites (shelf breaks), the low-mode dissipation in HYCOM is largely attributed to viscous damping (Fig. 5d). In deeper water, 2000–4500 m, the fraction of baroclinic dissipation due to wave drag is maximally 64%. Globally, roughly half the low-mode dissipation is due to internal wave drag (Fig. 1b). We argue that the internal tide damping is fairly well parameterized by the wave drag because the M_2 internal tide sea surface amplitudes of HYCOM computed for five, important, low-mode generation sites, including French Polynesia, agree with altimetry-derived amplitudes [see Table 2 of Shriver et al. (2012)]. In agreement with our findings, their altimetry-derived amplitude is 1.05 times larger than the HYCOM amplitude for the Polynesian Islands. For all five hotspot areas defined in Shriver et al. (2012), the altimetry-derived amplitudes of Shriver et al. (2012) are on average 1.06 times larger than the HYCOM amplitudes. For the Shriver et al. (2012) comparisons, SSH time series have been used ranging from 1 (HYCOM) to 17 yr (altimetry). Ansong et al. (2015) showed that internal tide sea surface height amplitudes from least squares fits decrease to an equilibrium value for time series longer than ~3 yr. Hence, the HYCOM amplitudes of Shriver et al. (2012) may be up to 5% larger than their equilibrium values, meaning that the equilibrium values in the HYCOM 18.5 simulation utilized in Shriver et al. (2012) and here may be about 10% smaller than the altimeter values. A drawback of using M_2 tides for the comparison is that we cannot differentiate between real internal tide dissipation and the loss of coherence. It seems that the combined effect of these two processes on the internal tides is reasonably well simulated in HYCOM, at least where global integrals are concerned. We assume that this is also the case for the individual processes.

This study shows that the details of wave–wave interaction processes, topographic scattering, and internal wave breaking for far-field internal tides are not well represented in relatively coarse-resolution global ocean models, like the one utilized here, and that these processes need to be parameterized. Our results in this regard are also in accordance with Niwa and Hibiya (2014), who applied linear damping terms to baroclinic velocities, temperature, and salinity to dampen the far-field internal waves in their global model.

Although not shown for the sake of brevity, the low-mode dissipation for M_2 internal tides in HYCOM agrees in magnitude and spatial distribution with the low-mode dissipation rates computed with the mathematical Internal Wave Dissipation, Energy and Mixing (IDEMIX) model (Olbers and Eden 2013; Eden and Olbers 2014). The IDEMIX model simulates the far-field dissipation of low modes due to topographic scattering and wave–wave interaction processes. It is promising that two entirely different models yield qualitatively similar answers. This is another confirmation that the low-mode dissipation is fairly well parameterized in HYCOM.

The application of an internal wave drag to the bottom 500 m in HYCOM affects both the surface and internal tides. Yet, the drag strength here has only been tuned to obtain the best possible surface tides, as in Arbic et al. (2004, 2010, 2012). Our analysis of the barotropic energetics suggests that the wave drag strength may have been too large. If this is correct, we have been somewhat fortunate with our choices regarding, for example, the wave drag scheme, the application of the wave drag over the bottom 500 m, and the amplification factor of 12. In future model simulations, we will examine whether wave drag terms specifically designed for surface and internal tides can be tuned independently.

It may be that HYCOM is slightly too dissipative, as the predicted internal tide amplitudes are smaller than inferred from altimetry (Figs. 10g,h). Nevertheless, the spatial distribution of the dissipation rates in HYCOM agrees reasonably well with the Argo dissipation rates and with the largest values occurring at rough topography (Fig. 8). Because the Argo data are sparse and are affected by nontidal processes, it is difficult for us to draw more definitive conclusions about the HYCOM–Argo comparison. HYCOM also seems too dissipative compared to other model studies. The low-mode dissipation as a fraction of the conversion $q = \{D_l\}/\{C\}$ in HYCOM near steep topography, such as in Luzon Strait, is about 60% (Fig. 5). These q values are about twice as large as found in the tide-only simulations of Luzon Strait by Buijsman et al. (2014) (2 km resolution and 50 layers) and Kerry et al. (2013) (4.5 km × 8 km and 25 layers). Kerry et al. (2013, 2014) performed numerical model simulations of the South China and Philippine Seas with tides only and simulations with tides and mesoscale circulation. Averaged over time, they find $q = 36\%$ for the former and $q = 41\%$ for the latter for
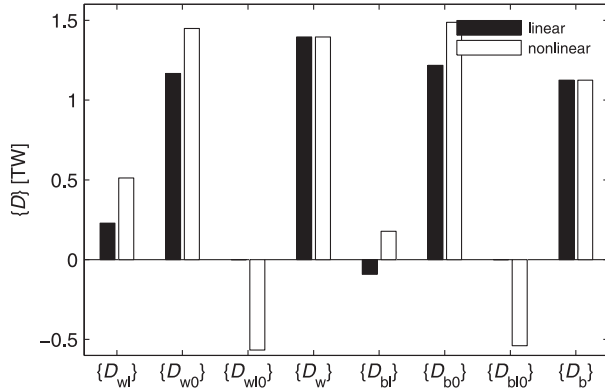
FIG. A1. The globally integrated and time-mean baroclinic and barotropic terms of the wave and bottom drag dissipation according to the linear (blue) and nonlinear (red) separations. The cross terms in the nonlinear split are D_{wl0} and D_{bl0}, respectively.

Luzon Strait (C. Kerry 2015, personal communication). While the inclusion of mesoscale circulation increases the internal tide dissipation rates due to the enhanced vertical shear (Kerry et al. 2014), their q is still smaller than in HYCOM. The higher rates in HYCOM may be attributed to the linear wave drag and the relatively coarse resolution of ~ 8 km.

Using the plane-wave fitting technique, we find that about 12% of the low-mode energy generated at deep-water sites propagates across the ~ 4000-m isobaths into the coastal regions. This value can be considered a lower-bound estimate because HYCOM slightly underpredicts the internal wave amplitudes. It is also lower than the 31% value found by Waterhouse et al. (2014).

If the internal tide decay in global ocean models can be correctly predicted, then these models can inform us about the locations of internal tide dissipation. This is relevant for the development of internal tide mixing parameterizations in climate models because their strength and location can affect the overturning circulation (Simmons et al. 2004b; Melet et al. 2013).

model data. This paper represents a contribution to the Internal Wave Mixing Climate Process Team (CPT), an NSF-funded project led by J. MacKinnon of the University of California in San Diego. J. K. Ansong, B. K. Arbic, M. C. Buijsman, C. B. Whalen, and Z. Zhao are regular participants in CPT meetings. The satellite altimeter products used in this study were produced by Ssalto/Duacs and distributed by AVISO, with support from CNES (http://www.aviso.altimetry.fr). The derived satellite altimetric internal tide products are available from Z. Zhao upon request.

APPENDIX

Linear versus Nonlinear Separation in Dissipation

In the nonlinear separation, we insert $u = u_l + u_0$ and $v = v_l + v_0$ in Eqs. (8) and (11), yielding

$$D_b = \langle \rho_0 C_D |u_a| (u_{la} u_{la} + v_{la} v_{la} + u_0 u_0 \\ + v_0 v_0 + 2 u_0 u_{la} + 2 v_0 v_{la}) \rangle, \qquad (A1)$$

and

$$D_w = \langle \rho_0 \mathbb{C}(u_{la} u_{la} + v_{la} v_{la} + u_0 u_0 + v_0 v_0 + 2 u_0 u_{la} + 2 v_0 v_{la}) \rangle. \qquad (A2)$$

In Eqs. (A1) and (A2), the first two terms within the parentheses contribute to the baroclinic part and the third and fourth terms contribute to the barotropic part of the dissipation. The last two terms are referred to as the cross terms, contributing to D_{bl0} and D_{wl0}.

We compare the linear and nonlinear separation of the time-mean and globally integrated barotropic and baroclinic wave and bottom drag dissipation rates in Fig. A1. The barotropic dissipation due to wave and quadratic drag are the largest terms and have the same order of magnitude in both the linear and nonlinear separation, implying that the barotropic dissipation is well defined. In contrast, the baroclinic wave and bottom drag terms are smaller and differ by a factor of 2 and/or a sign. While the baroclinic wave drag is reasonably well defined in both separations, that is, they have the same sign and spatial patterns (not shown), the baroclinic bottom drag dissipation is mostly negative in the linear separation and positive in the nonlinear separation. The negative dissipation is the result of the anticorrelation of the baroclinic with the barotropic velocities. The cross terms for the wave and bottom drag have an equal magnitude, but they are generally of a larger magnitude than the baroclinic dissipation rates.

REFERENCES

Alford, M. H., and Coauthors, 2011: Energy flux and dissipation in Luzon Strait: Two tales of two ridges. *J. Phys. Oceanogr.*, **41**, 2211–2222, doi:10.1175/JPO-D-11-073.1.

——, and Coauthors, 2015: The formation and fate of internal waves in the South China Sea. *Nature*, **521**, 65–69, doi:10.1038/nature14399.

Ansong, J. K., B. K. Arbic, M. C. Buijsman, J. G. Richman, J. F. Shriver, and A. J. Wallcraft, 2015: Indirect evidence for substantial damping of low-mode internal tides in the open ocean. *J. Geophys. Res. Oceans*, **120**, 6057–6071, doi:10.1002/2015JC010998.

Arbic, B. K., S. T. Garner, R. W. Hallberg, and H. L. Simmons, 2004: The accuracy of surface elevations in forward global barotropic and baroclinic tide models. *Deep-Sea Res. II*, **51**, 3069–3101, doi:10.1016/j.dsr2.2004.09.014.

——, A. Wallcraft, and E. Metzger, 2010: Concurrent simulation of the eddying general circulation and tides in a global ocean model. *Ocean Modell.*, **32**, 175–187, doi:10.1016/j.ocemod.2010.01.007.

——, J. Richman, J. Shriver, P. Timko, E. J. Metzger, and A. J. Wallcraft, 2012: Global modeling of internal tides within an eddying ocean general circulation model. *Oceanography*, **25**, 20–29, doi:10.5670/oceanog.2012.38.

Bell, T. H., 1975: Topographically generated internal waves in the open ocean. *J. Geophys. Res.*, **80**, 320–327, doi:10.1029/JC080i003p00320.

Bleck, R., 2002: An oceanic general circulation model framed in hybrid isopycnic Cartesian coordinates. *Ocean Modell.*, **4**, 55–88, doi:10.1016/S1463-5003(01)00012-9.

Buijsman, M. C., C. Jackson, and J. C. McWilliams, 2010: East-west asymmetry in nonlinear internal waves from Luzon Strait. *J. Geophys. Res.*, **115**, C10057, doi:10.1029/2009JC006004.

——, S. Legg, and J. Klymak, 2012: Double-ridge internal tide interference and its effect on dissipation in Luzon Strait. *J. Phys. Oceanogr.*, **42**, 1337–1356, doi:10.1175/JPO-D-11-0210.1.

——, and Coauthors, 2014: Three-dimensional double-ridge internal tide resonance in Luzon Strait. *J. Phys. Oceanogr.*, **44**, 850–869, doi:10.1175/JPO-D-13-024.1.

——, B. K. Arbic, J. A. M. Green, R. W. Helber, J. G. Richman, J. F. Shriver, P. G. Timko, and A. J. Wallcraft, 2015: Optimizing internal wave drag in a forward barotropic model with semidiurnal tides. *Ocean Modell.*, **85**, 42–55, doi:10.1016/j.ocemod.2014.11.003.

Dunphy, M., and K. G. Lamb, 2014: Focusing and vertical mode scattering of the first mode internal tide by mesoscale eddy interaction. *J. Geophys. Res. Oceans*, **119**, 523–536, doi:10.1002/2013JC009293.

Eden, C., and D. Olbers, 2014: An energy compartment model for propagation, nonlinear interaction, and dissipation of internal gravity waves. *J. Phys. Oceanogr.*, **44**, 2093–2106, doi:10.1175/JPO-D-13-0224.1.

Egbert, G. D., and R. D. Ray, 2001: Estimates of M^2 tidal energy dissipation from TOPEX/Poseidon altimeter data. *J. Geophys. Res.*, **106**, 22 475–22 502, doi:10.1029/2000JC000699.

——, and ——, 2003: Semi-diurnal and diurnal tidal dissipation from TOPEX/Poseidon altimetry. *Geophys. Res. Lett.*, **30**, 1907, doi:10.1029/2003GL017676.

——, A. Bennett, and M. Foreman, 1994: TOPEX/Poseidon tides estimated using a global inverse model. *J. Geophys. Res.*, **99**, 24 821–24 852, doi:10.1029/94JC01894.

——, R. D. Ray, and B. G. Bills, 2004: Numerical modeling of the global semidiurnal tide in the present day and in the Last Glacial Maximum. *J. Geophys. Res.*, **109**, C03003, doi:10.1029/2003JC001973.

Falahat, S., J. Nycander, F. Roquet, and M. Zarroug, 2014: Global calculation of tidal energy conversion into vertical normal modes. *J. Phys. Oceanogr.*, **44**, 3225–3244, doi:10.1175/JPO-D-14-0002.1.

Garner, S. T., 2005: A topographic drag closure built on an analytical base flux. *J. Atmos. Sci.*, **62**, 2302–2315, doi:10.1175/JAS3496.1.

Green, J. A. M., and J. Nycander, 2013: A comparison of tidal conversion parameterizations for tidal models. *J. Phys. Oceanogr.*, **43**, 104–119, doi:10.1175/JPO-D-12-023.1.

Hallberg, R., 2005: A thermobaric instability of Lagrangian vertical coordinate ocean models. *Ocean Modell.*, **8**, 279–300, doi:10.1016/j.ocemod.2004.01.001.

——, and P. Rhines, 1996: Buoyancy-driven circulation in an ocean basin with isopycnals intersecting the sloping boundary. *J. Phys. Oceanogr.*, **26**, 913–940, doi:10.1175/1520-0485(1996)026<0913:BDCIAO>2.0.CO;2.

Jayne, S. R., and L. C. St. Laurent, 2001: Parameterizing tidal dissipation over rough topography. *Geophys. Res. Lett.*, **28**, 811–814, doi:10.1029/2000GL012044.

Kang, D., and O. Fringer, 2012: Energetics of barotropic and baroclinic tides in the Monterey Bay area. *J. Phys. Oceanogr.*, **42**, 272–290, doi:10.1175/JPO-D-11-039.1.

Kelly, S. M., and J. D. Nash, 2010: Internal-tide generation and destruction by shoaling internal tides. *Geophys. Res. Lett.*, **37**, L23611, doi:10.1029/2010GL045598.

——, N. L. Jones, J. D. Nash, and A. F. Waterhouse, 2013: The geography of semidiurnal mode-1 internal-tide energy loss. *Geophys. Res. Lett.*, **40**, 4689–4693, doi:10.1002/grl.50872.

Kerry, C., B. Powell, and G. Carter, 2013: Effects of remote generation sites on model estimates of M_2 internal tides in the Philippine Sea. *J. Phys. Oceanogr.*, **43**, 187–204, doi:10.1175/JPO-D-12-081.1.

——, ——, and ——, 2014: The impact of subtidal circulation on internal-tide-induced mixing in the Philippine Sea. *J. Phys. Oceanogr.*, **44**, 3209–3224, doi:10.1175/JPO-D-13-0249.1.

Klymak, J. M., R. Pinkel, and L. Rainville, 2008: Direct breaking of the internal tide near topography: Kaena Ridge, Hawaii. *J. Phys. Oceanogr.*, **38**, 380–399, doi:10.1175/2007JPO3728.1.

Legg, S., and J. Klymak, 2008: Internal hydraulic jumps and overturning generated by tidal flow over a tall steep ridge. *J. Phys. Oceanogr.*, **38**, 1949–1964, doi:10.1175/2008JPO3777.1.

Lyard, F., F. Lefevre, T. Letellier, and O. Francis, 2006: Modelling the global ocean tides: Modern insights from FES2004. *Ocean Dyn.*, **56**, 394–415, doi:10.1007/s10236-006-0086-x.

MacKinnon, J. A., M. H. Alford, R. Pinkel, J. M. Klymak, and Z. Zhao, 2013: The latitudinal dependence of shear and mixing in the Pacific transiting the critical latitude for PSI. *J. Phys. Oceanogr.*, **43**, 3–16, doi:10.1175/JPO-D-11-0107.1.

Martini, K. I., M. H. Alford, E. Kunze, S. M. Kelly, and J. D. Nash, 2011: Observations of internal tides on the Oregon continental slope. *J. Phys. Oceanogr.*, **41**, 1772–1794, doi:10.1175/2011JPO4581.1.

Mathur, M., G. S. Carter, and T. Peacock, 2014: Topographic scattering of the low-mode internal tide in the deep ocean. *J. Geophys. Res. Oceans*, **119**, 2165–2182, doi:10.1002/2013JC009152.

Melet, A., R. Hallberg, S. Legg, and K. Polzin, 2013: Sensitivity of the ocean state to the vertical distribution of internal-tide-driven mixing. *J. Phys. Oceanogr.*, **43**, 602–615, doi:10.1175/JPO-D-12-055.1.

Metzger, E. J., H. E. Hurlburt, X. Xu, J. F. Shriver, A. L. Gordon, J. Sprintall, R. D. Susanto, and H. M. van Aken, 2010: Simulated and observed circulation in the Indonesian Seas: 1/12° global HYCOM and the INSTANT observations. *Dyn. Atmos. Oceans*, **50**, 275–300, doi:10.1016/j.dynatmoce.2010.04.002.

Müller, M., J. Cherniawsky, M. Foreman, and J.-S. von Storch, 2012: Global map of M_2 internal tide and its seasonal variability from high resolution ocean circulation and tide modelling. *Geophys. Res. Lett.*, **39**, L19607, doi:10.1029/2012GL053320.

Munk, W., and C. Wunsch, 1998: Abyssal recipes II: Energetics of tidal and wind mixing. *Deep-Sea Res.*, **45**, 1977–2010, doi:10.1016/S0967-0637(98)00070-3.

Nash, J. D., E. Kunze, J. M. Toole, and R. W. Schmitt, 2004: Internal tide reflection and turbulent mixing on the continental slope. *J. Phys. Oceanogr.*, **34**, 1117–1134, doi:10.1175/1520-0485(2004)034<1117:ITRATM>2.0.CO;2.

Niwa, Y., and T. Hibiya, 2011: Estimation of baroclinic tide energy available for deep ocean mixing based on three-dimensional global numerical simulations. *J. Oceanogr.*, **67**, 493–502, doi:10.1007/s10872-011-0052-1.

——, and ——, 2014: Generation of baroclinic tide energy in a global three-dimensional numerical model with different spatial grid resolutions. *Ocean Modell.*, **80**, 59–73, doi:10.1016/j.ocemod.2014.05.003.

Nycander, J., 2005: Generation of internal waves in the deep ocean by tide. *J. Geophys. Res.*, **110**, C10028, doi:10.1029/2004JC002487.

Olbers, D., and C. Eden, 2013: A global model for the diapycnal diffusivity induced by internal gravity waves. *J. Phys. Oceanogr.*, **43**, 1759–1779, doi:10.1175/JPO-D-12-0207.1.

Polzin, K. L., 2004: Idealized solutions for the energy balance of the finescale internal wave field. *J. Phys. Oceanogr.*, **34**, 231–246, doi:10.1175/1520-0485(2004)034<0231:ISFTEB>2.0.CO;2.

Ponte, A. L., and P. Klein, 2015: Incoherent signature of internal tides on sea level in idealized numerical simulations. *Geophys. Res. Lett.*, **42**, 1520–1526, doi:10.1002/2014GL062583.

Ray, R. D., 1998: Ocean self-attraction and loading in numerical tidal models. *Mar. Geod.*, **21**, 181–192, doi:10.1080/01490419809388134.

——, and G. T. Mitchum, 1997: Surface manifestation of internal tides in the deep ocean: Observations from altimetry and island gauges. *Prog. Oceanogr.*, **40**, 135–162, doi:10.1016/S0079-6611(97)00025-6.

Rosmond, T. E., J. Teixeira, M. Peng, T. F. Hogan, and R. Pauley, 2002: Navy Operational Global Atmospheric Prediction System (NOGAPS): Forcing for ocean models. *Oceanography*, **15**, 99–108, doi:10.5670/oceanog.2002.40.

Shriver, J. F., B. K. Arbic, J. G. Richman, R. D. Ray, E. J. Metzger, A. J. Wallcraft, and P. G. Timko, 2012: An evaluation of the barotropic and internal tides in a high resolution global ocean circulation model. *J. Geophys. Res.*, **117**, C10024, doi:10.1029/2012JC008170.

——, J. G. Richman, and B. K. Arbic, 2014: How stationary are the internal tides in a high-resolution global ocean circulation model? *J. Geophys. Res. Oceans*, **119**, 2769–2787, doi:10.1002/2013JC009423.

Simmons, H. L., R. W. Hallberg, and B. K. Arbic, 2004a: Internal wave generation in a global baroclinic tide model. *Deep-Sea Res. II*, **51**, 3043–3068, doi:10.1016/j.dsr2.2004.09.015.

——, S. R. Jayne, L. C. St. Laurent, and A. J. Weaver, 2004b: Tidally driven mixing in a numerical model of the ocean general circulation. *Ocean Modell.*, **6**, 245–263, doi:10.1016/S1463-5003(03)00011-8.

Stigebrandt, A., 1999: Resistance to barotropic tidal flow in straits by baroclinic wave drag. *J. Phys. Oceanogr.*, **29**, 191–197, doi:10.1175/1520-0485(1999)029<0191:RTBTFI>2.0.CO;2.

St. Laurent, L., and C. Garrett, 2002: The role of internal tides in mixing the deep ocean. *J. Phys. Oceanogr.*, **32**, 2882–2899, doi:10.1175/1520-0485(2002)032<2882:TROITI>2.0.CO;2.

——, H. L. Simmons, and S. R. Jayne, 2002: Estimating tidally driven mixing in the deep ocean. *Geophys. Res. Lett.*, **29**, 2106, doi:10.1029/2002GL015633.

Timko, P. G., B. K. Arbic, J. G. Richman, R. B. Scott, E. J. Metzger, and A. J. Wallcraft, 2012: Skill tests of three-dimensional tidal currents in a global ocean model: A look at the North Atlantic. *J. Geophys. Res.*, **117**, C08014, doi:10.1029/2011JC007617.

——, ——, ——, ——, ——, and ——, 2013: Skill testing a three-dimensional global tide model to historical current meter records. *J. Geophys. Res. Oceans*, **118**, 6914–6933, doi:10.1002/2013JC009071.

Waterhouse, A. F., and Coauthors, 2014: Global patterns of diapycnal mixing from measurements of the turbulent dissipation rate. *J. Phys. Oceanogr.*, **44**, 1854–1872, doi:10.1175/JPO-D-13-0104.1.

Whalen, C. B., L. D. Talley, and J. A. MacKinnon, 2012: Spatial and temporal variability of global ocean mixing inferred from Argo profiles. *Geophys. Res. Lett.*, **39**, L18612, doi:10.1029/2012GL053196.

——, J. A. MacKinnon, L. D. Talley, and A. F. Waterhouse, 2015: Estimating the mean diapycnal mixing using a finescale strain parameterization. *J. Phys. Oceanogr.*, **45**, 1174–1188, doi:10.1175/JPO-D-14-0167.1.

Zaron, E. D., and G. D. Egbert, 2014: Time-variable refraction of the internal tide at the Hawaiian Ridge. *J. Phys. Oceanogr.*, **44**, 538–557, doi:10.1175/JPO-D-12-0238.1.

Zhao, Z., M. H. Alford, J. A. MacKinnon, and R. Pinkel, 2010: Long-range propagation of the semidiurnal internal tide from the Hawaiian Ridge. *J. Phys. Oceanogr.*, **40**, 713–736, doi:10.1175/2009JPO4207.1.

——, M. Alford, and J. Girton, 2012: Mapping low-mode internal tides from multisatellite altimetry. *Oceanography*, **25**, 42–51, doi:10.5670/oceanog.2012.40.

Zilberman, N. V., J. M. Becker, M. A. Merrifield, and G. S. Carter, 2009: Model estimates of M_2 internal tide generation over Mid-Atlantic Ridge topography. *J. Phys. Oceanogr.*, **39**, 2635–2651, doi:10.1175/2008JPO4136.1.